Supplementary Information for

Observed pattern-effect contribution to recent warming from reduced aerosol emissions

Jianglei Xu[1], Shunlin Liang[1*], Han Ma[1], Yongzhe Chen[1], Wenyuan Li[1], Yichuan Ma[1], Yuxiang Zhang[1], Shikang Guang[1], Zhen Xiao[1], He Wang[1], Yngqian Ren[1]

1. Jockey Club Laboratory of Quantitative Remote Sensing, Department of Geography, University of Hong Kong, Hong Kong SAR, China

*Corresponding author:

shunlin@hku.hk

The content of this file includes

- Supplementary Figures 1–35
- Supplementary Tables 1–3
- Supplementary Texts 1–3

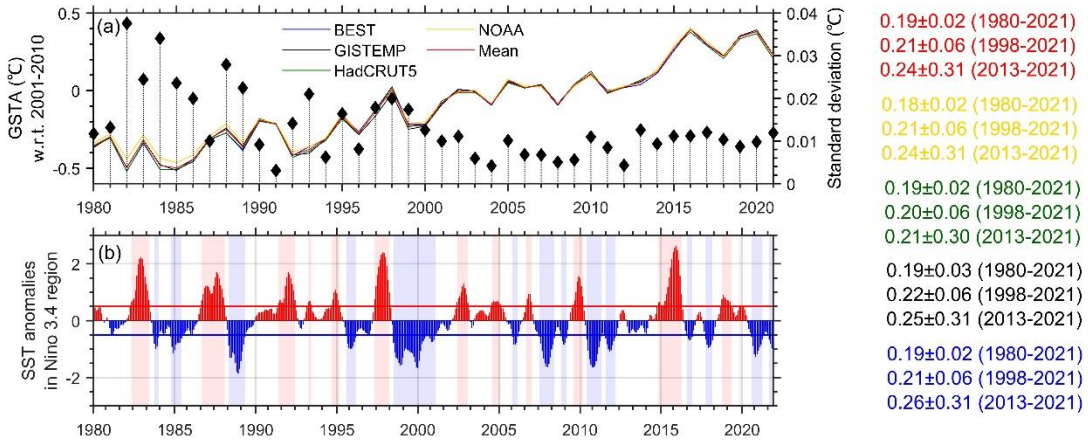

Supplementary Figure 1. Global surface air temperature anomalies and sea surface temperature anomalies in Nino 3.4 region (5N-5S, 120-170W). a, Global surface temperature anomalies relative to 2001-2010 from BEST, GISTEMP, HadCRUT5, NOAA, and their means during 1980-2021. The diamond line is the standard deviation between these air temperature products, representing the confidence level of the data at each year. **b**, Nino 3.4 sea surface temperature anomaly (°C) during 1980-2021. The red and bule shading areas represent El Nino or La Nina events with the NINO3.4 SST anomalies exceeding +/- 0.5°C during a period of six month. Surface warming rates for recent approximately 40-, 20-, and 10-year periods are given for reference (uncertainty given by 95% confidence interval).

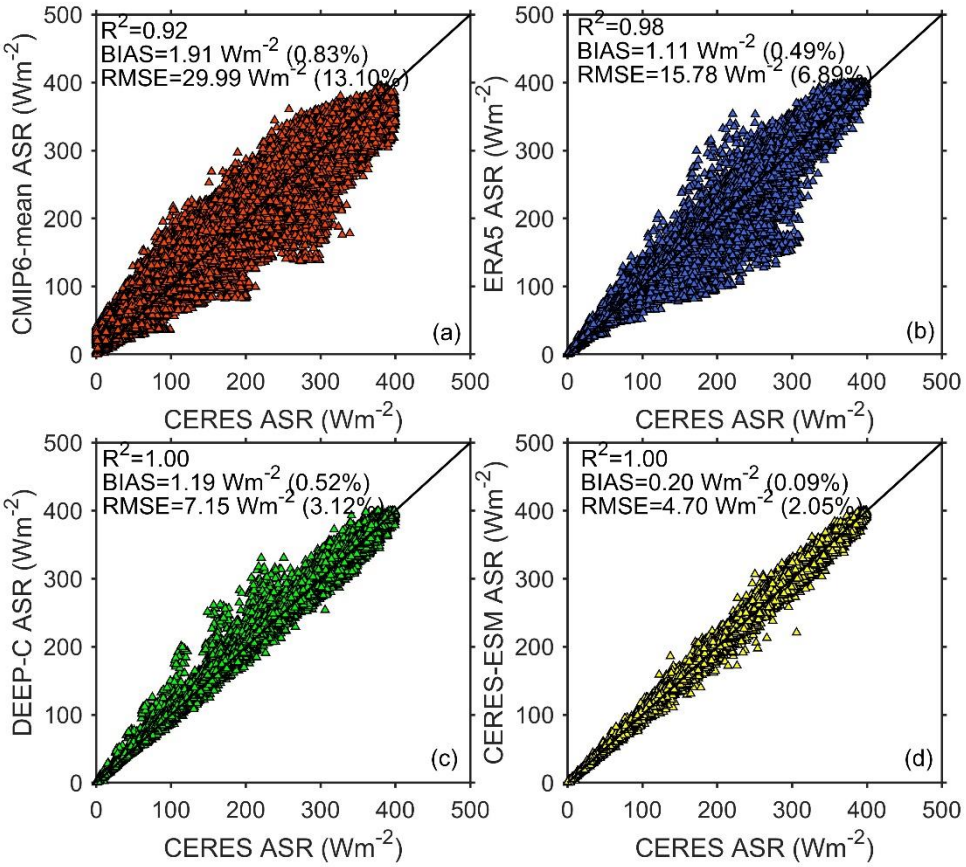

Supplementary Figure 2. Validation of monthly mean absorbed solar radiation (ASR) at top-of-atmosphere against CERES-EBAF data from an ensemble mean of CMIP6 (a), ERA5 (b), DEEP-C (c), and CERES-ESM (d). The coefficient of determination, bias, root mean square error, normalized bias, and normalized root mean square error are used to evaluate the accuracy performances of these four datasets by referencing the well-recognized CERES-EBAF product.

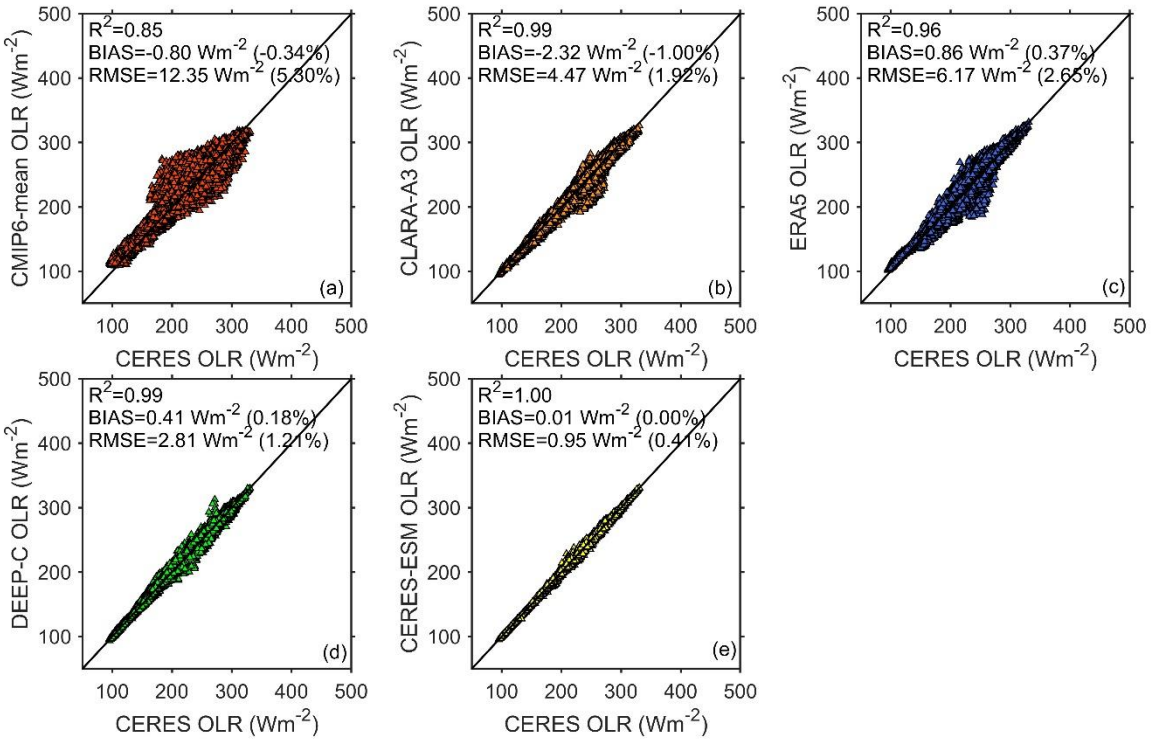

Supplementary Figure 3. Validation of monthly mean outgoing longwave radiation (OLR) at top-of-atmosphere against CERES-EBAF data from an ensemble mean of CMIP6 (a), CLARA-A3 (b), ERA5 (c), DEEP-C (d), and (e) CERES-ESM. The coefficient of determination, bias, root mean square error, normalized bias, and normalized root mean square error are used to evaluate the accuracy performances of these four datasets by referencing the well-recognized CERES-EBAF product.

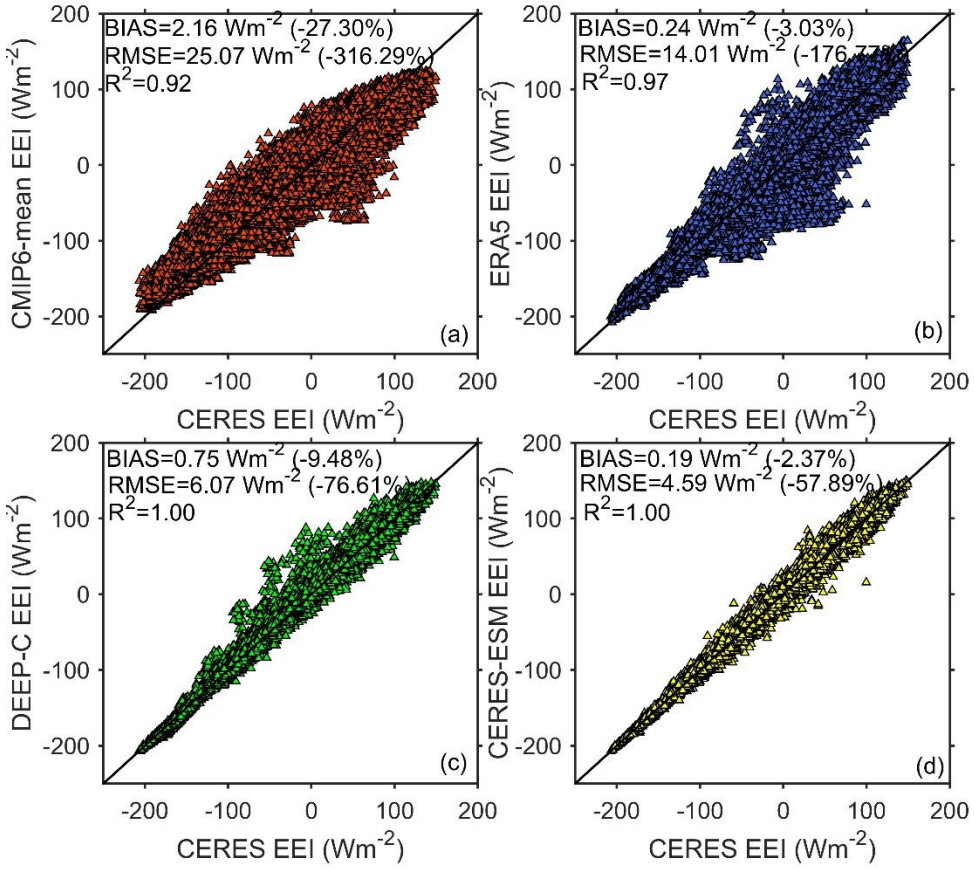

Supplementary Figure 4. Validation of monthly mean Earth energy imbalance (EEI) against CERES-EBAF data from an ensemble mean of CMIP6 (a), ERA5 (b), DEEP-C (c), and CERES-ESM (d). The coefficient of determination, bias, root mean square error, normalized bias, and normalized root mean square error are used to evaluate the accuracy performances of these four datasets by referencing the well-recognized CERES-EBAF product.

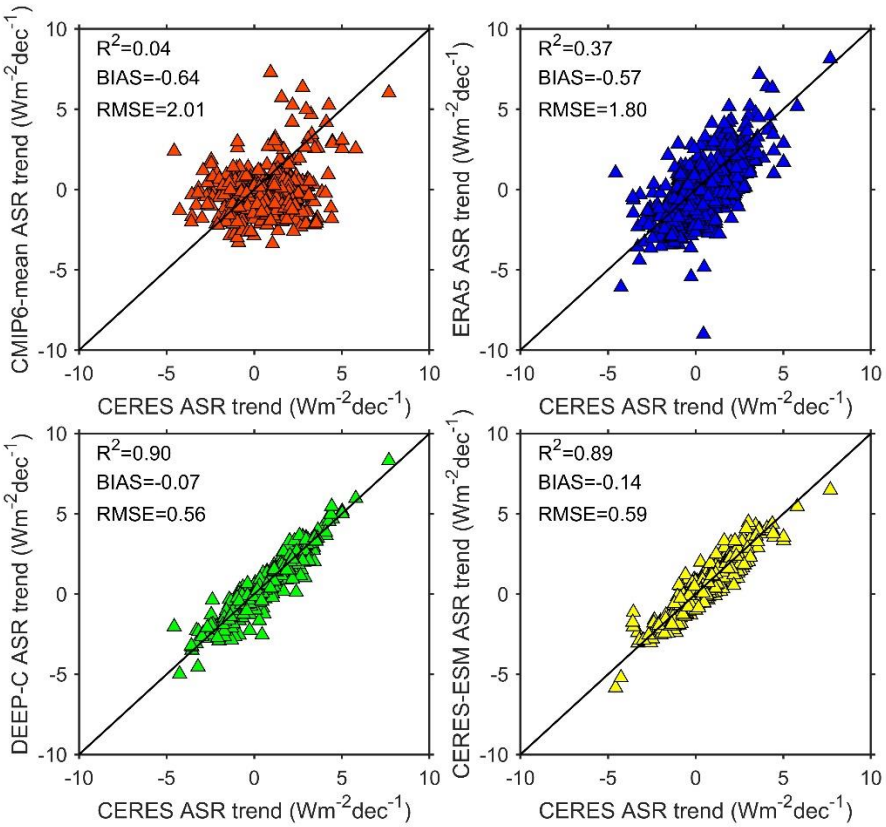

Supplementary Figure 5. Validation of trend in monthly mean absorbed solar radiation (ASR) at top-of-atmosphere against CERES-EBAF data at pixel scale (1 degree) from an ensemble mean of CMIP6 (a), ERA5 (b), DEEP-C (c), and CERES-ESM (d). The coefficient of determination, bias, and root mean square error are used to evaluate the accuracy performances of these four datasets by referencing the well-recognized CERES-EBAF product.

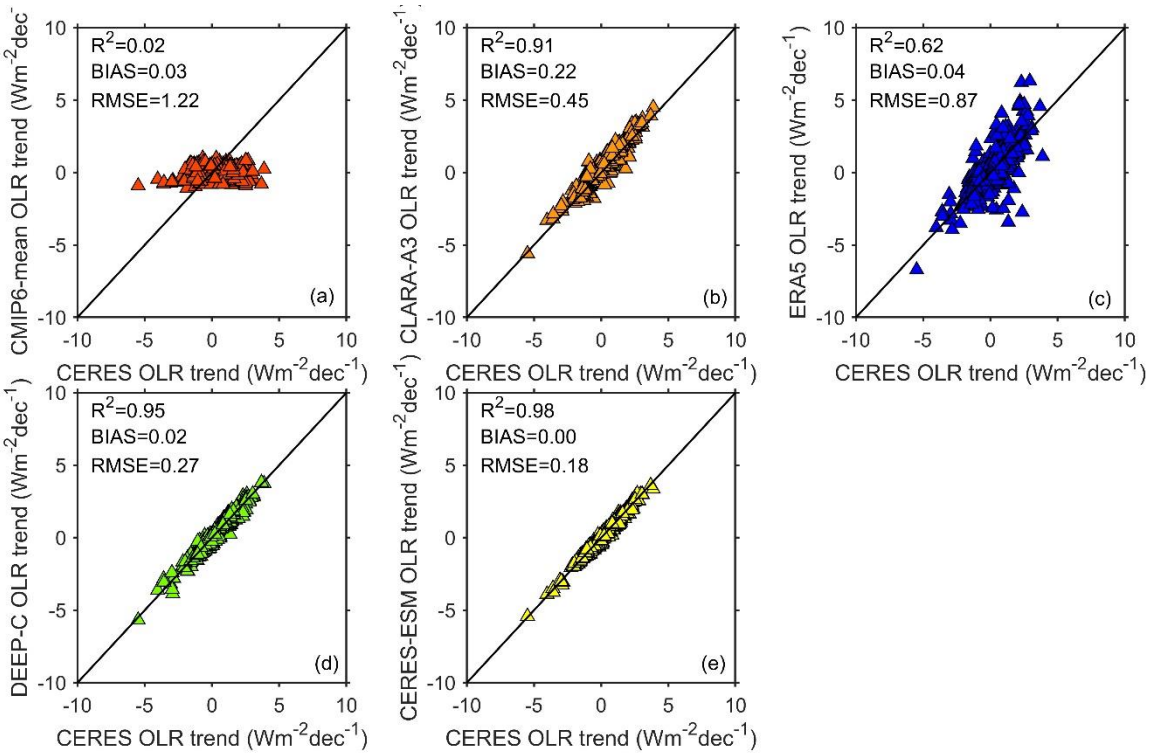

Supplementary Figure 6. Validation of trend in monthly mean outgoing longwave radiation (OLR) at top-of-atmosphere against CERES-EBAF data at pixel scale (1 degree) from an ensemble mean of CMIP6 (a), CLARA-A3 (b), ERA5 (c), DEEP-C (d), and CERES-ESM (e). The coefficient of determination, bias, and root mean square error are used to comprehensively evaluate the accuracy performances of these four datasets by referencing the well-recognized CERES-EBAF product.

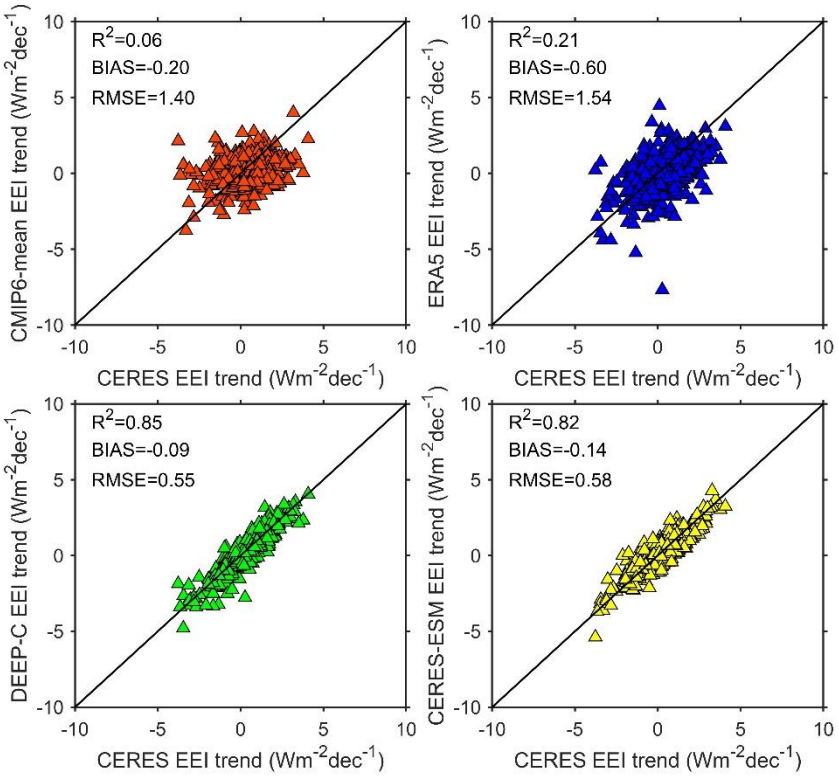

Supplementary Figure 7. Validation of trend in monthly mean Earth energy imbalance (EEI) against CERES-EBAF data at pixel scale (1 degree) from an ensemble mean of CMIP6 (a), ERA5 (b), DEEP-C (c), and CERES-ESM (d). The coefficient of determination, bias, and root mean square error are used to comprehensively evaluate the accuracy performances of these four datasets by referencing the well-recognized CERES-EBAF product.

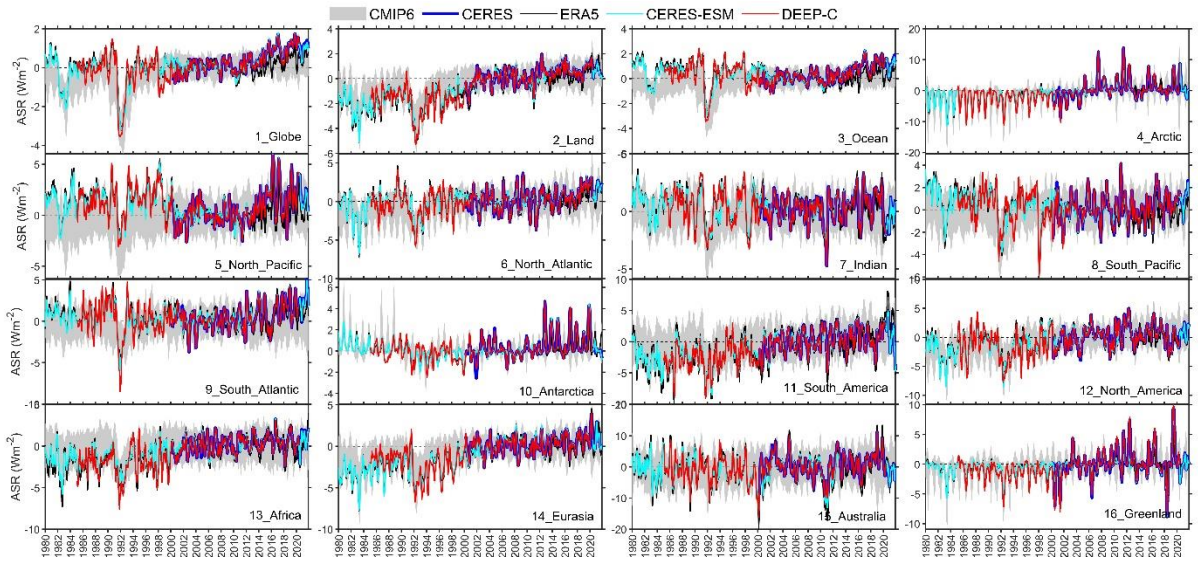

Supplementary Figure 8. Absorbed solar radiation (ASR) anomalies relative to 2001-2010 at global and regional scales from CMIP6 ensemble, CERES-EBAF, ERA5, CERES-ESM, and DEEP-C products. The globe was divided into 13 subregions to fully investigate the temporal variability of CERESW-ESM ASR by referencing other EEB datasets, including Arctic, North Pacific, North Atlantic, Indian, South Pacific, South Atlantic, Antarctica, South America, North America, Africa, Eurasia, Australia, and Greenland. The division of subregions is based on continents and ocean basins for NASA energy and water cycle study climatology (https://dx.doi.org/10.5067/7VZB10AK8S3D).

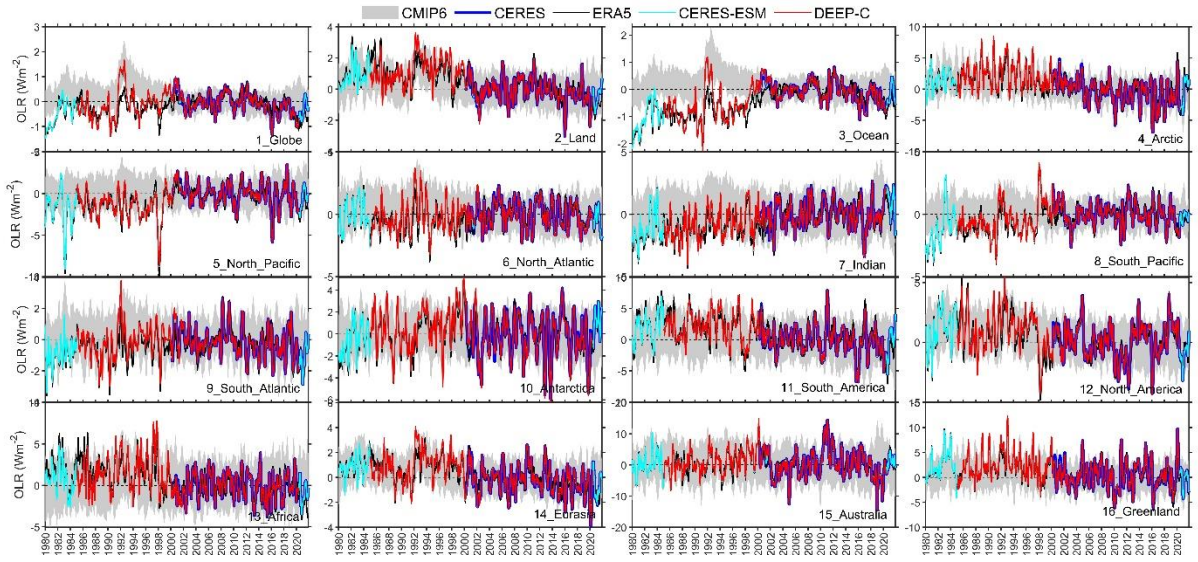

Supplementary Figure 9. Outgoing longwave radiation (OLR) anomalies relative to 2001-2010 at global and regional scales from CMIP6 ensemble, CERES-EBAF, ERA5, CERES-ESM, and DEEP-C products. The globe was divided into 13 subregions to fully investigate the temporal variability of CERESW-ESM ASR by referencing other TOA EEB datasets, including Arctic, North Pacific, North Atlantic, Indian, South Pacific, South Atlantic, Antarctica, South America, North America, Africa, Eurasia, Australia, and Greenland. The division of subregions is based on continents and ocean basins for NASA energy and water cycle study climatology (https://dx.doi.org/10.5067/7VZB10AK8S3D).

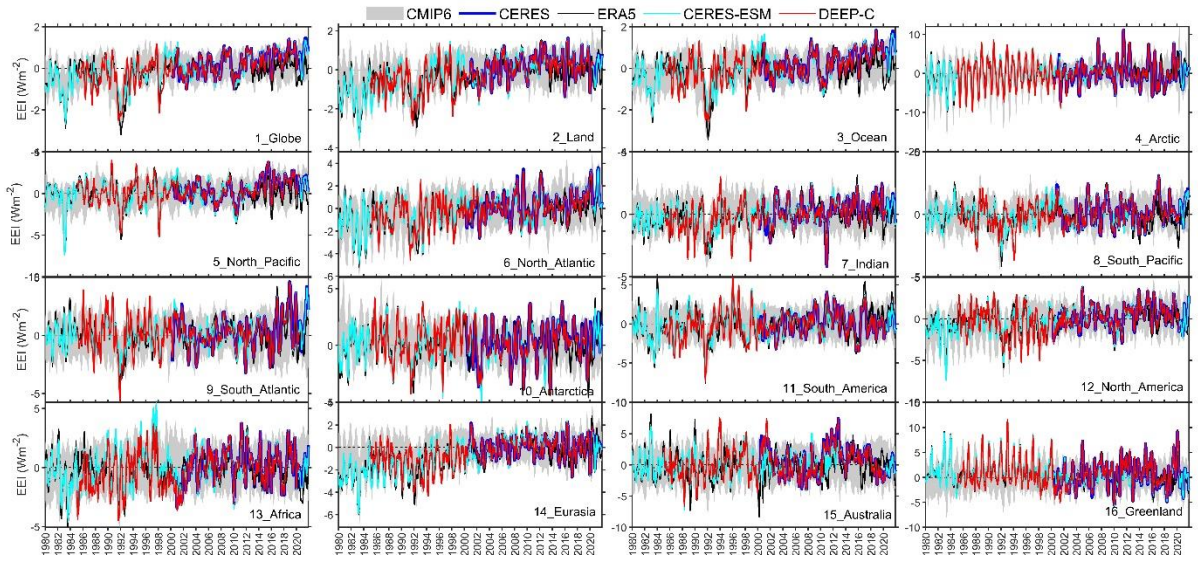

Supplementary Figure 10. Earth energy imbalance (EEI) anomalies relative to 2001-2010 at global and regional scales from CMIP6 ensemble, CERES-EBAF, ERA5, CERES-ESM, and DEEP-C products. The globe was divided into 13 subregions to fully investigate the temporal variability of CERESW-ESM ASR by referencing other TOA EEB datasets, including Arctic, North Pacific, North Atlantic, Indian, South Pacific, South Atlantic, Antarctica, South America, North America, Africa, Eurasia, Australia, and Greenland. The division of subregions is based on continents and ocean basins for NASA energy and water cycle study climatology (https://dx.doi.org/10.5067/7VZB10AK8S3D).

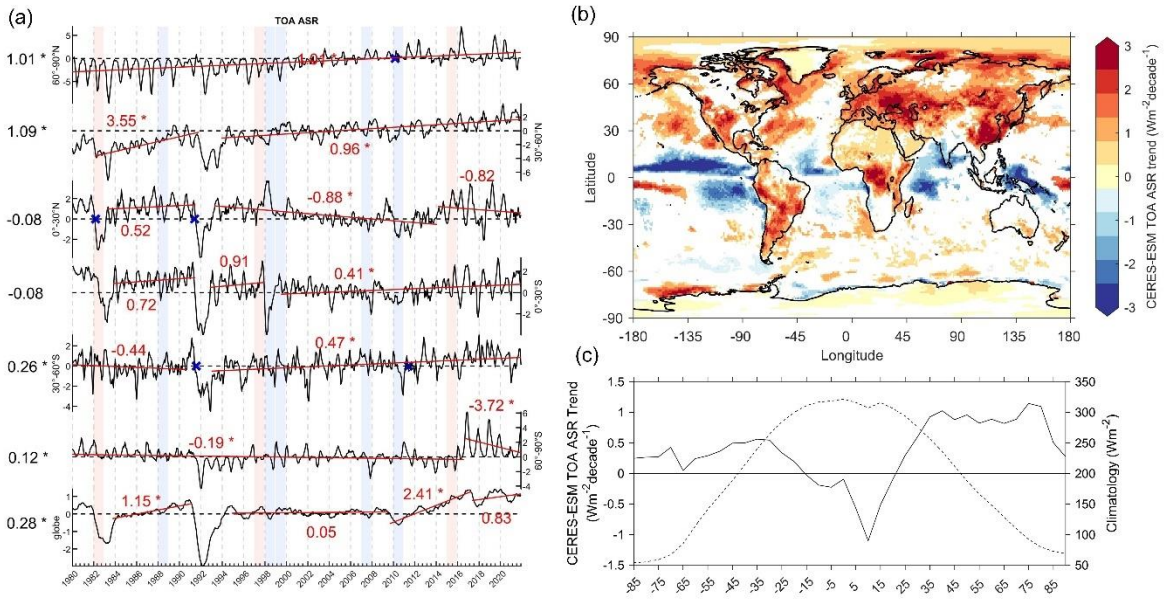

Supplementary Figure 11. Spatiotemporal variations of CERES-ESM absorbed solar radiation (ASR) at top of atmosphere between 1980 and 2021. a, temporal profiles of ASR at different latitudinal zones (30° interval) across the globe. The red lines are segmented trends with significant turning points at two adjacent periods. The left numbers show the 40-yr trends of ASR at different latitudinal zones. The asterisk means the trend is significant at the 95% confidence level (F statistic, $p < 0.05$). **b**, spatial distribution of trends in ASR between 1980 and 2021. Only significant trends are displayed. **c,** trends and climatology in ASR across latitudes. Zonal mean climatology is dotted, linear trend is solid, circles indicate trend statistical significance ($p < 0.05$). TOA radiative fluxes are defined as positive downwards.

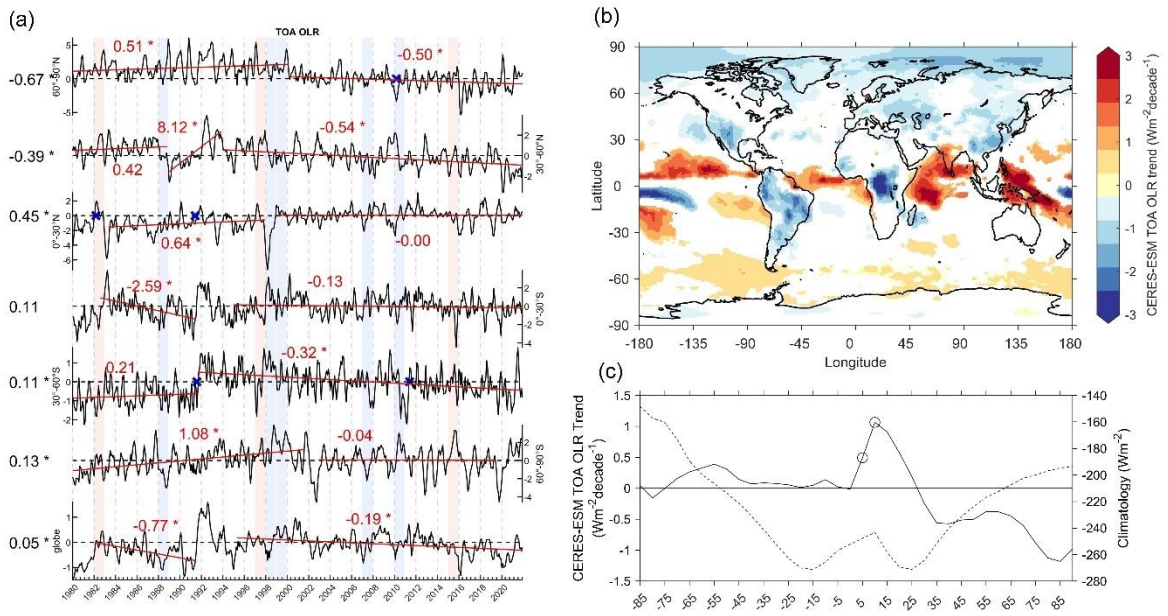

Supplementary Figure 12. Spatiotemporal variations of CERES-ESM outgoing longwave radiation (OLR) at top of atmosphere between 1980 and 2021. a, temporal profiles of OLR at different latitudinal zones (30° interval) across the globe. The red lines are segmented trends with significant turning points at two adjacent periods. The left numbers show the 40-yr trends of OLR at different latitudinal zones. The asterisk means the trend is significant at the 95% confidence level (F statistic, $p < 0.05$). **b**, spatial distribution of trends in OLR between 1980 and 2021. Only significant trends are displayed. **c,** trends and climatology in OLR across latitudes. Zonal mean climatology is dotted, linear trend is solid, circles indicate trend statistical significance ($p < 0.05$). TOA radiative fluxes are defined as positive downwards.

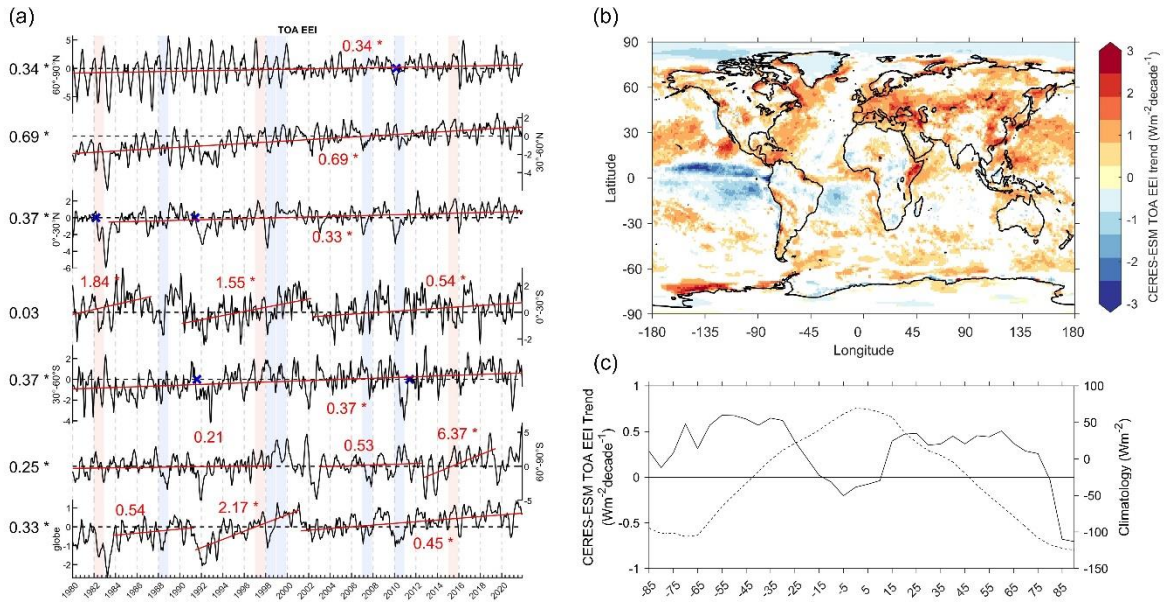

Supplementary Figure 13. Spatiotemporal variations of CERES-ESM Earth energy imbalance (EEI) at top of atmosphere between 1980 and 2021. a, temporal profiles of EEI at different latitudinal zones (30° interval) across the globe. The red lines are segmented trends with significant turning points at two adjacent periods. The left numbers show the 40-yr trends of EEI at different latitudinal zones. The asterisk means the trend is significant at the 95% confidence level (*F* statistic, $p < 0.05$). **b**, spatial distribution of trends in EEI between 1980 and 2021. Only significant trends are displayed. **c**, trends and climatology in EEI across latitudes. Zonal mean climatology is dotted, linear trend is solid, circles indicate trend statistical significance ($p < 0.05$). TOA radiative fluxes are defined as positive downwards.

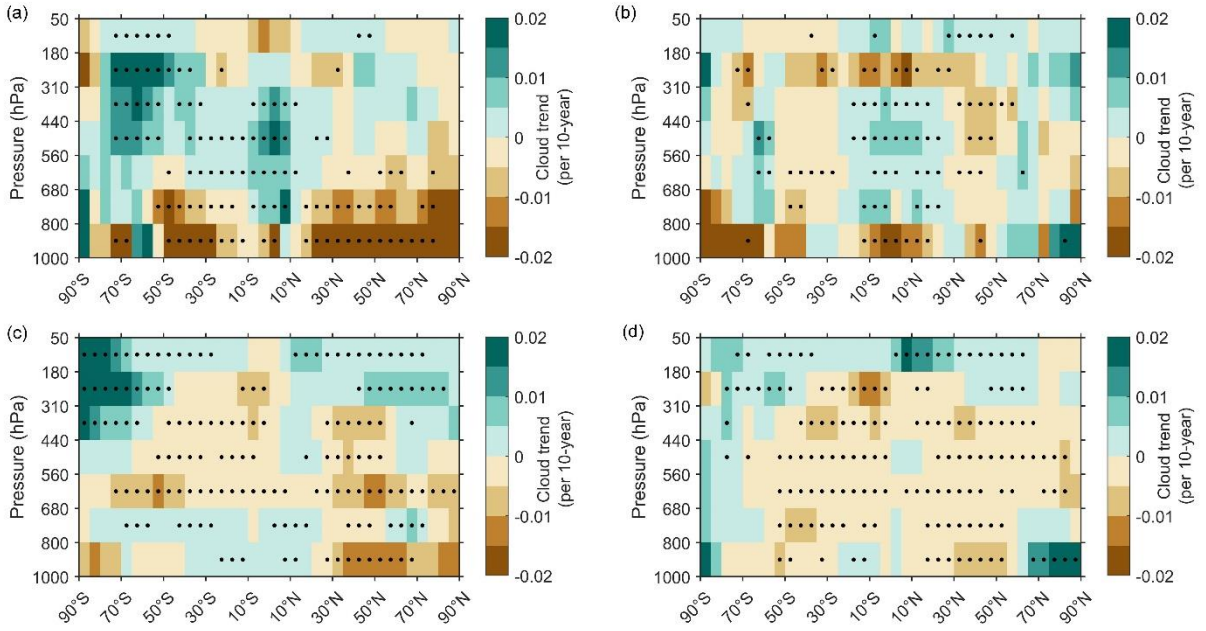

Supplementary Figure 14. Zonal mean change in observed and simulated cloud amount during the period 1980-2000 and 2001-2021 in seven pressure intervals. a, trends in ERA5 cloud amount 1980-2000. **b,** trends in ERA5 cloud amount 2001-2021. **c,** trend in ensemble mean cloud amount 1980–2000 from CMIP6 historical simulations with all radiative forcings. **d,** trend in ensemble mean cloud amount 2001–2021 from CMIP6 historical simulations with all radiative forcings. Black dots indicate trend statistical significance ($P < 0.05$).

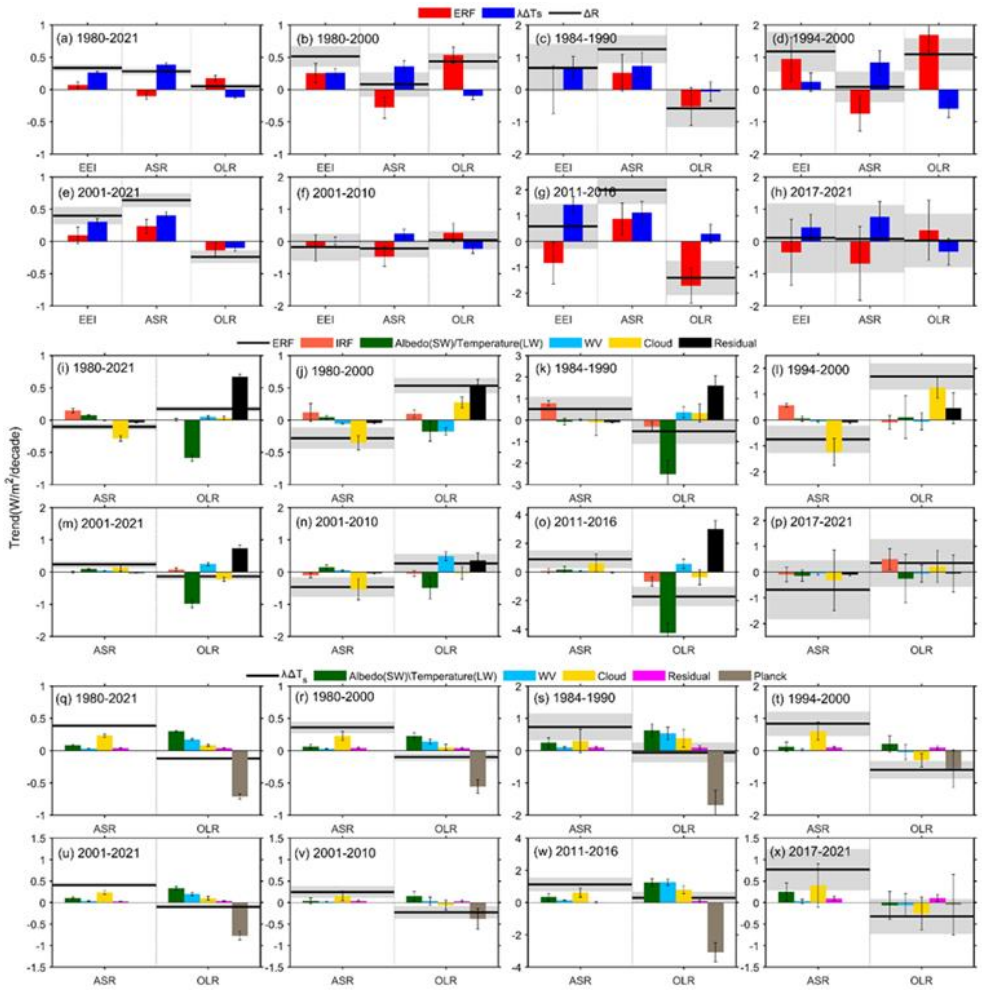

Supplementary Figure 15. Decomposition of Earth's energy budget (EEB) trends at different periods into radiative forcings, climate responses, and their respective mechanisms. a-h, segmented trends of effective radiative forcing and climate response in the EEI, ASR, and OLR components. **i-p,** segmented trends of ERF and its different mechanisms in ASR and OLR components. **q-x,** segmented trends of climate response and its different mechanisms in ASR and OLR components. Trends are calculated from deseasonalized CERES-ESM EEB monthly values. Anomalies are calculated relative to climatology over the period 2001-2010. TOA radiative fluxes are defined as positive downwards. EEB anomalies are decomposed into effective radiative forcings (*ERF*) and climate responses ($\boldsymbol{\lambda\Delta T_s}$). ERF is the sum of instantaneous radiative forcings (*IRF*) and rapid adjustments of different mechanisms ($\boldsymbol{\Delta A_x}$) due to atmospheric temperature (T), water vapor (q), surface albedo ($\boldsymbol{\alpha}$), clouds (C), and residuals accounting for nonlinearities. Climate response is the sum of mechanisms associated with albedo, lapse rate, water vapor, clouds, Planck, and residuals originating from atmospheric heat transport and the oceanic heat exchange. The grey shading shows a 5–95% confidence interval. Whiskers of the bar represent the 95% confidence intervals. The segmented periods are determined by referring to the temporal shifts of EEB fluxes from Supplementary Figures. 11(a)–13(a).

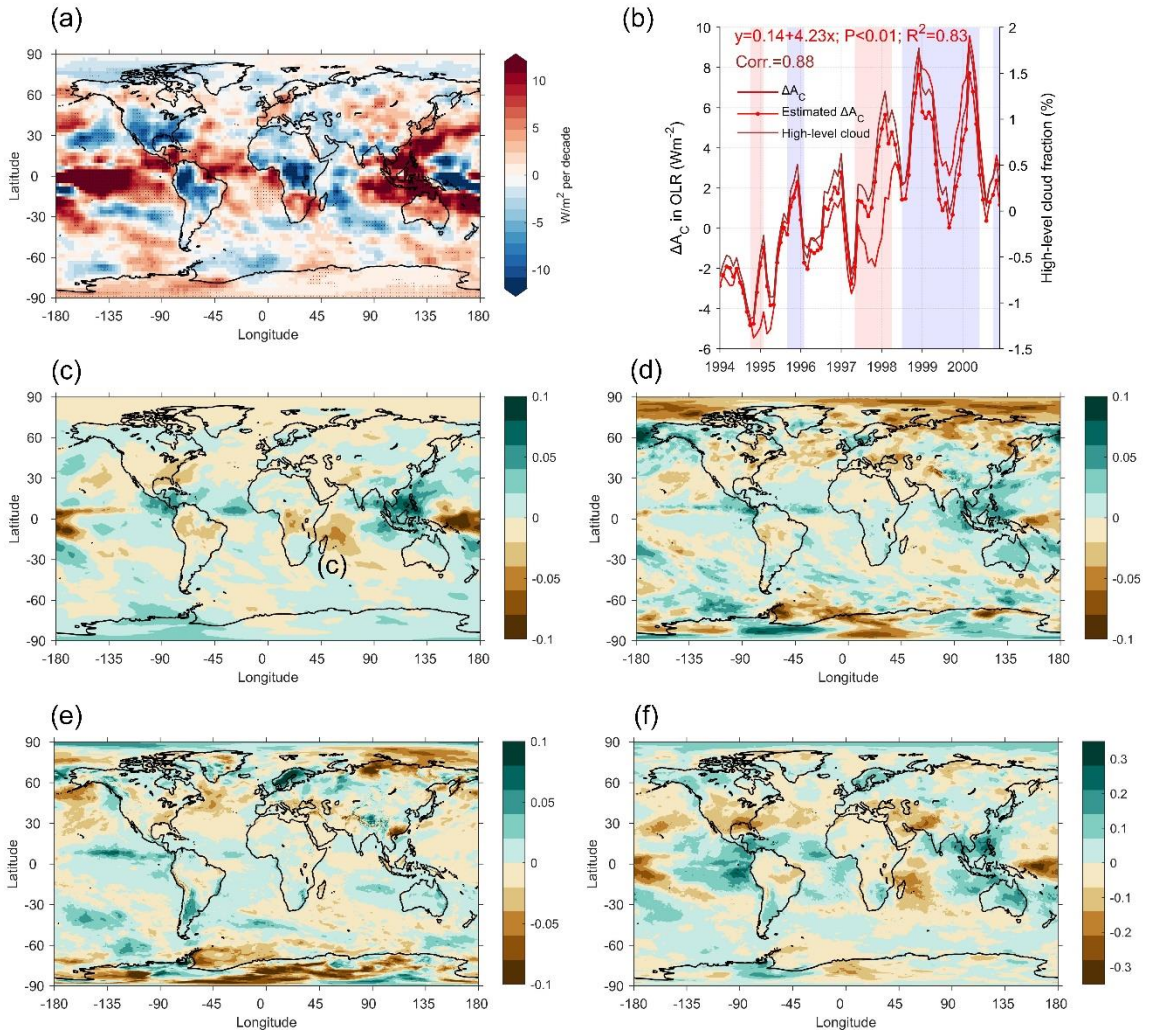

Supplementary Figure 16. Spatial distributions of trend in ΔA_C in OLR and cloud cover for the period of 1994-2000. a, trends of ΔA_C in OLR. The dot represents the significant trend at 95% confidence level. **b**, temporal variations of high-cloud cover, ΔA_C, and estimated ΔA_C from high-cloud cover based on a linear regression model. **c**, trends of high-level cloud cover. **d**, trends of middle-level cloud cover. **e**, trends of low-level cloud cover. **f**, trends of total cloud cover. The estimated ΔA_C is calculate from the linear regression model using high-level cloud cover as independent variable. The high-, middle-, and low-level cloud covers are classified as those at pressures of 10-440, 440-680, and 680-1000 hPa, respectively, following the same definitions in the ISCCP. The red and blue shadings represent the onset of El Nino and La Nina. A strong correlation between observed and estimated ΔA_C demonstrates the significance of high-cloud cover in rapid adjustment process responding for the 1997–2000 ENSO perturbation.

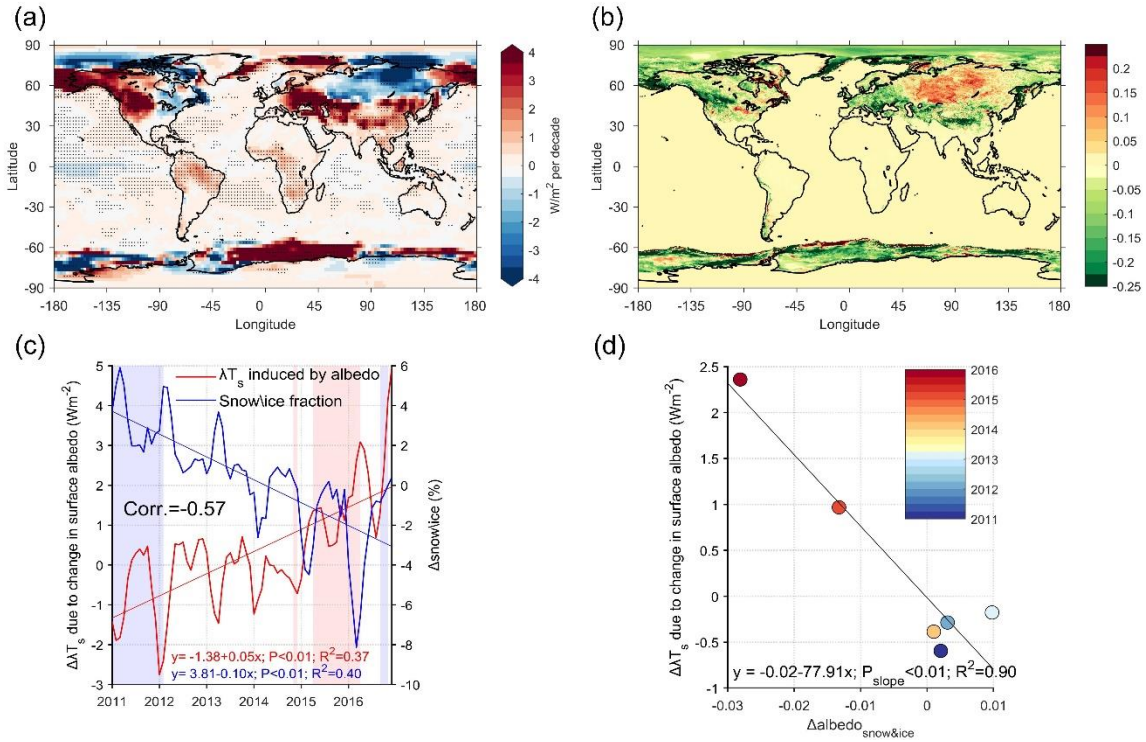

Supplementary Figure 17. Variations of snow/ice cover and radiative response ($\lambda\Delta T_s$) of ASR induced by change in surface albedo during 2011-2016. a. spatial distribution of trends in surface albedo-induced ASR change in the radiative response process. **b.** spatial distribution of trends in snow and ice cover. **c.** temporal variations in anomalies of snow/ice cover and albedo-induced ASR change in radiative response process. **d.** scatter plot of snow/ice cover and albedo-induced ASR change in radiative response process as a function of year. The red and bule shading areas represent El Nino or La Nina events with the NINO3.4 SST anomalies exceeding +/- 0.6 °C.

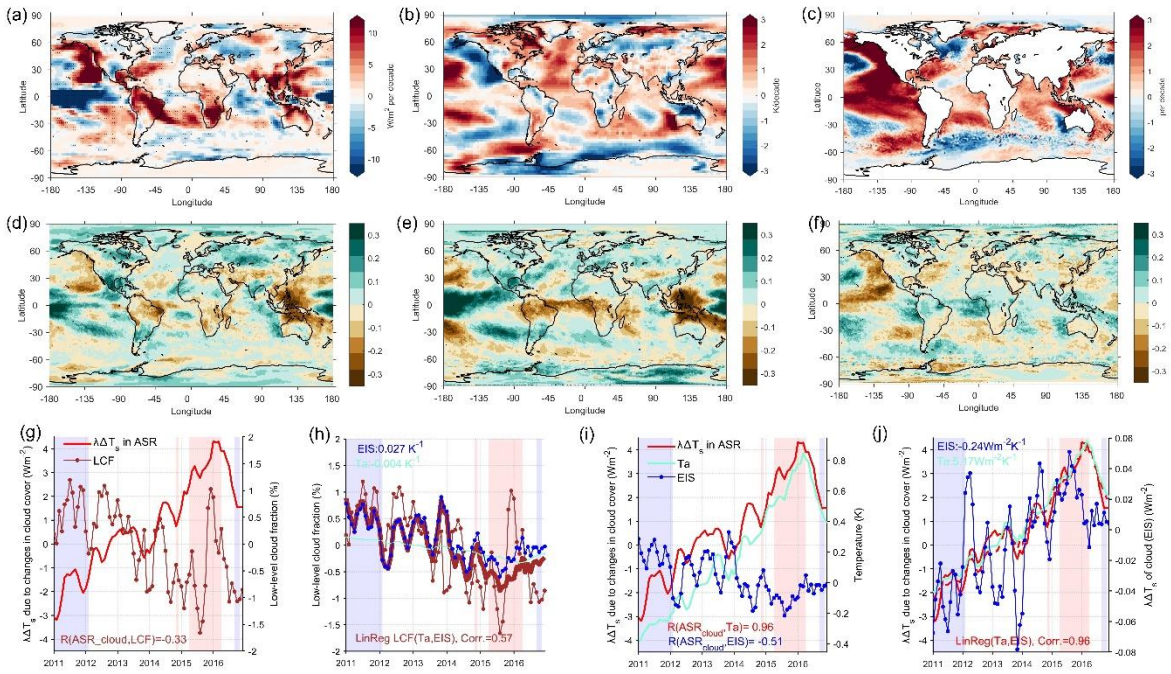

Supplementary Figure 18. Variations of ASR in cloud shortwave radiative response, estimated inversion strength, sea surface temperature, low- and high-level cloud cover during 2011-2016. a. spatial distribution of trends in ASR in cloud shortwave radiative response. **b**. spatial distribution of trends in estimated inversion strength (EIS). **c**. spatial distribution of trends in sea surface temperature. **d, e, f**. spatial distribution of trends in total, low-level, and high-level cloud covers. **g**. time series of cloud-indued radiative response and low-level cloud cover. **h**. time series of low-level cloud cover (brown dotted line), linearly estimated low-level cloud cover using surface air temperature (T_a) and (EIS) (brown bold line; LCF = *f* (Ta, EIS)), and T_a and EIS multiplied with their slopes $dLCF/dT_a$ (green line) and *dLCF/dEIS* (blue dotted line) of the multiple linear regression. **i.** time series of cloud-indued radiative response, Ta, and EIS. **j**. time series of cloud-indued radiative response (red solid line), linearly estimated radiative response (red dashed line) using T_a and EIS (red dashed line, $\boldsymbol{\lambda\Delta T_s}$ = *f* (T_a, EIS)), and T_a and EIS multiplied with their slopes $d\boldsymbol{\lambda\Delta T_s}/dT_a$ (green line) and $d\boldsymbol{\lambda\Delta T_s}/dEIS$ (blue dotted line) of the multiple linear regression. The red and bule shading areas represent El Nino or La Nina events with the NINO3.4 SST anomalies exceeding +/- 0.6 °C.

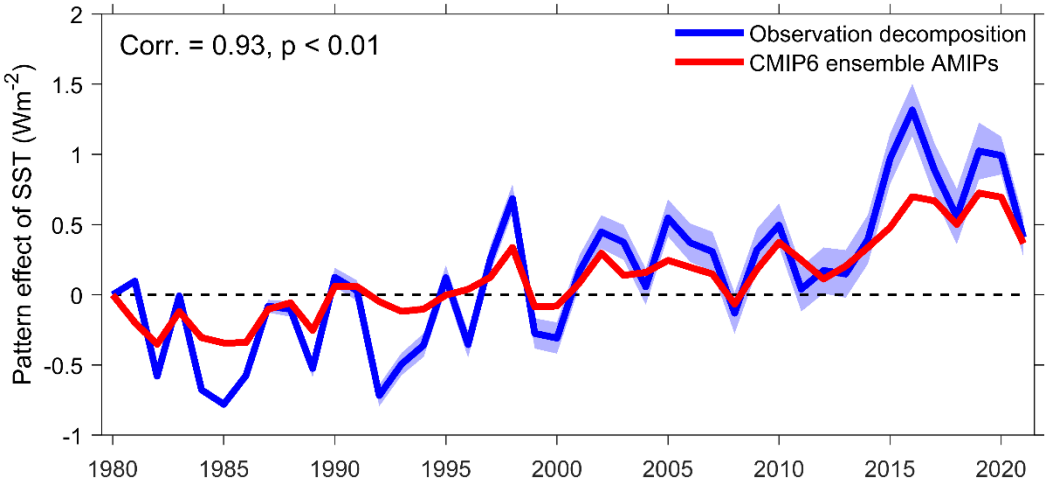

Supplementary Figure 19. Temporal variations of TOA outgoing longwave radiation calculated from radiative kernel-based decomposition and CMP6 AMIP-series models, including AMIP, AMIP-p4k, and AMIP-future4k experiments. The result from radiative kernel-based decomposition is obtained from Figure 2d. Regarding results based on CMIP6 AMIP-series models, we first calculated the feedback parameter of the SST pattern effect from AMIP, AMIP-p4k, and AMIP-future4k experiments. Then, we calculated the change in OLR due to ocean warming by using the model-derived feedback parameter and air temperature observation to extend the historical simulations (ending in 2014) into the year 2021.

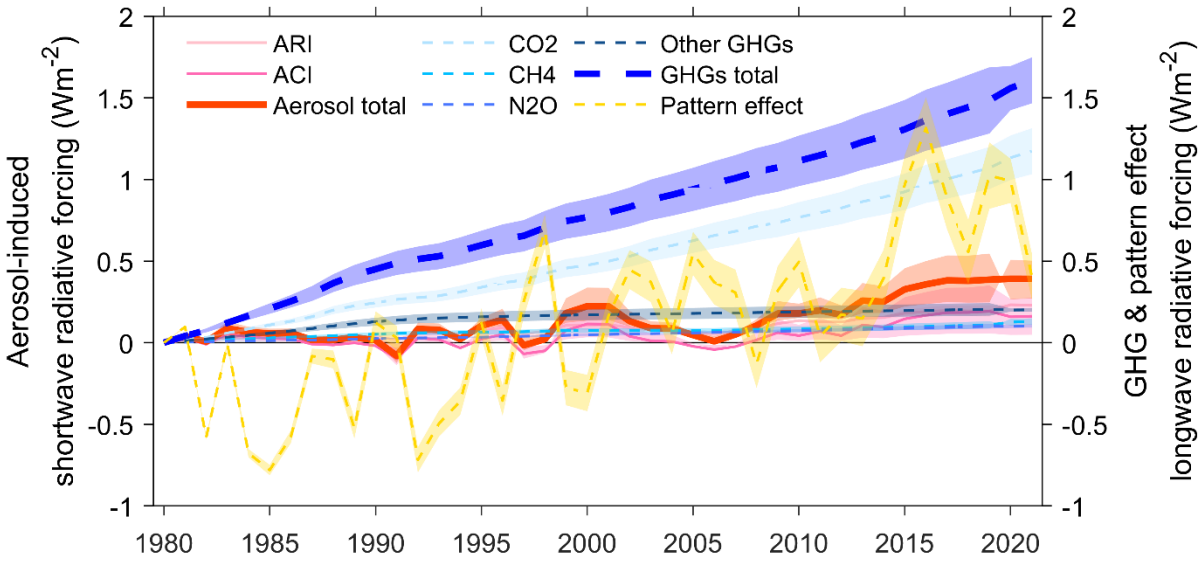

Supplementary Figure 20. Temporal variations of anthropogenic radiative forcings from the IPCC AR6[1]. The shortwave radiative forcing**s** include mechanisms of aerosol-radiation interaction (ARI), aerosol-cloud interaction (ACI), and aerosol total (ARI+ACI). The longwave radiative forcing includes of GHGs (CO2, CH4, N2O, and other GHGs) and pattern effect of sea surface warming and sea ice. The shaded area represents the 5th-95th confidence interval. The time series of anomalies are relative to 1980.

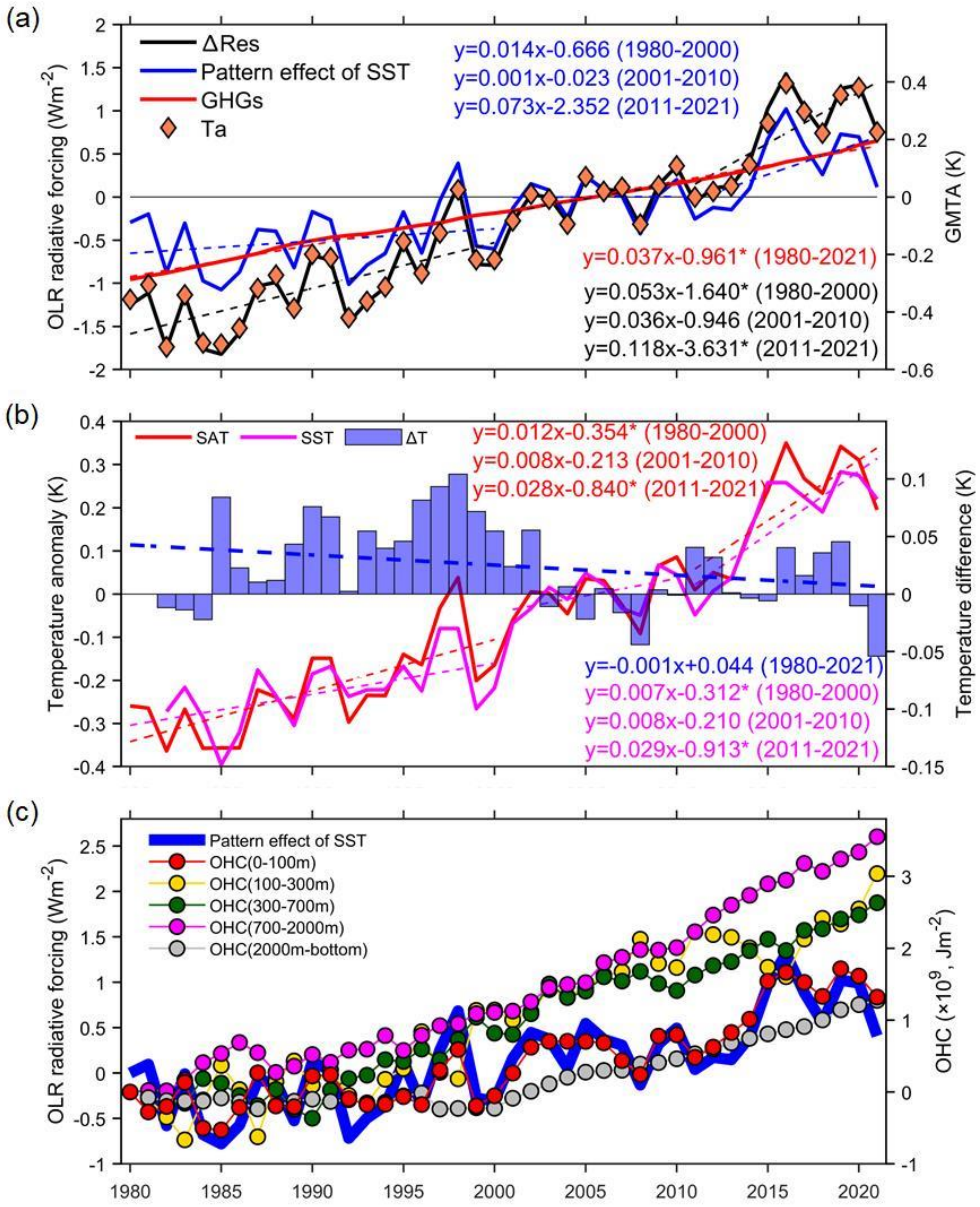

Supplementary Figure 21. Time series of temperature, ocean heat content, and pattern effect of SST warming from 1980 to 2021. a, temporal variations of longwave radiative forcing anomalies from residual item, pattern effect of SST warming, and GHG emissions. Temporal variation of global mean surface air temperature anomalies is also presented. **b,** temporal variations of surface air temperature and sea surface temperature anomalies. The difference between these two items is included. The linear variations of each item are provided during three periods, including 1980-2000, 2001-2010, and 2011-2021. The asterisk means the trend is significant at the 95% confidence level (F statistic, $p < 0.05$). **c,** temporal variabilities of ocean heat contents (OHCs) at different depths and radiation forcing due to internal the pattern effect of SST warming. The land area has been masked in the T_a. Anomalies are calculated relative to the climatology of 2001-2010.

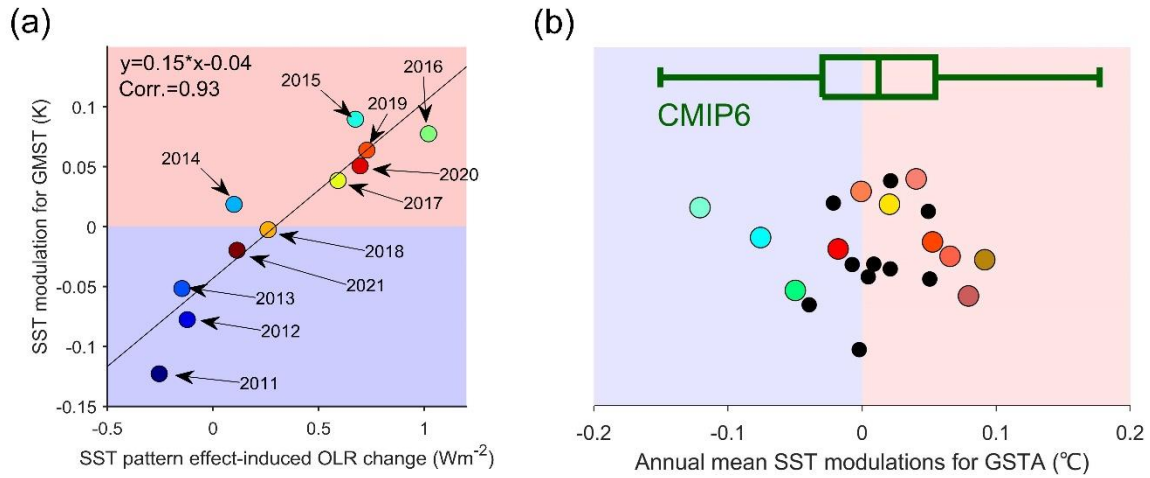

Supplementary Figure 22. Sea surface temperature modulation for global mean surface temperature due to the pattern effect of sea surface temperature. a, annual mean pattern effect of SST versus GMST modulation due to the SST pattern quantified via a Green's Function using observations and climate models. The years are indicated in text. The error bar represents the standard deviations of SST modulations for the GMST across climate models. The linear regression and correlation are also given. **b**, annual SST modulation factors during 2001-2021, for CMIP6 (box-and-whisker) and observations (points). Modulation years since 2011 are shown in colors, and black dots represent the SST modulation during 2001-2010. Red and bule areas represent warming and cooling effects of the SST modulations for the GMST.

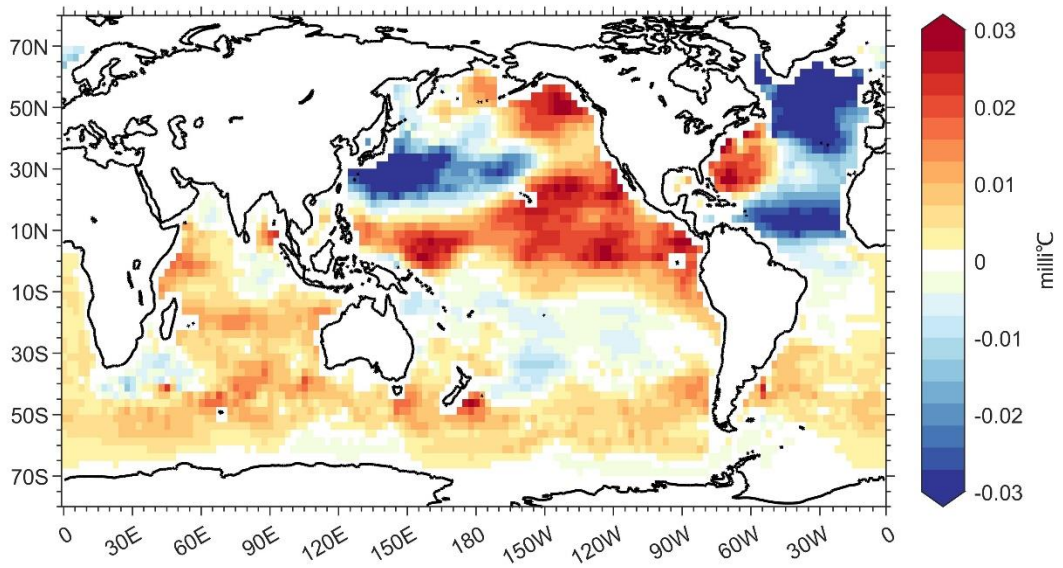

Supplementary Figure 23. Spatial distribution of mean sea surface temperature modulations for global mean surface temperature during the 2011-2021 period. Red (bule) areas represent the contributions of warming (cooling) modulations for the GMST from sea surface temperature change.

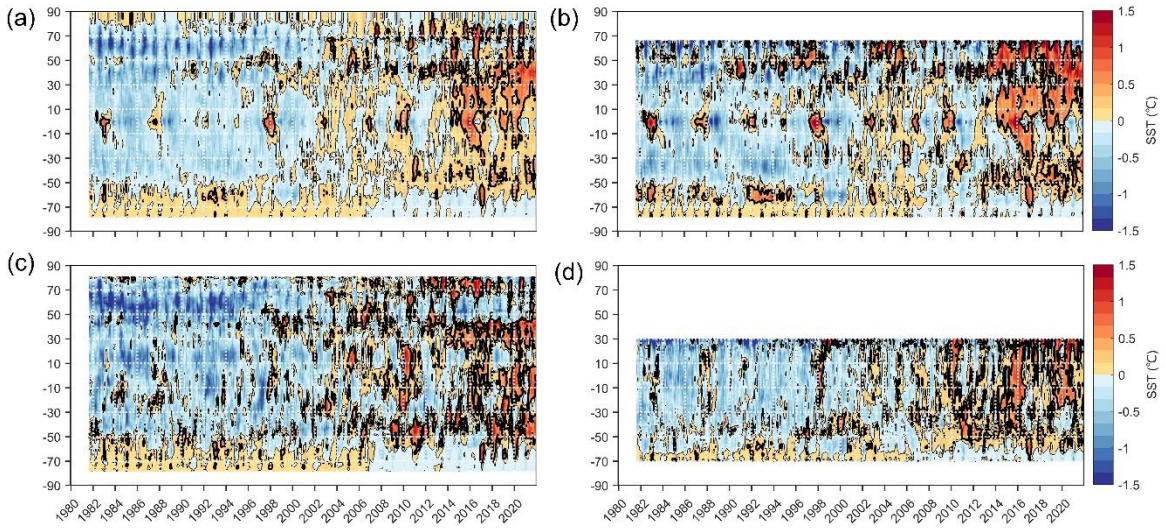

Supplementary Figure 24. Zonal mean variations of sea surface temperature (SST) anomalies relative to 2001-2010 at different ocean basins. a, Global oceans. **b,** Pacific oceans. **c,** Atlantic oceans. **d,** Indian oceans. The thick black lines highlight the significant increase of SST, with increased magnitudes of > 0.5K.

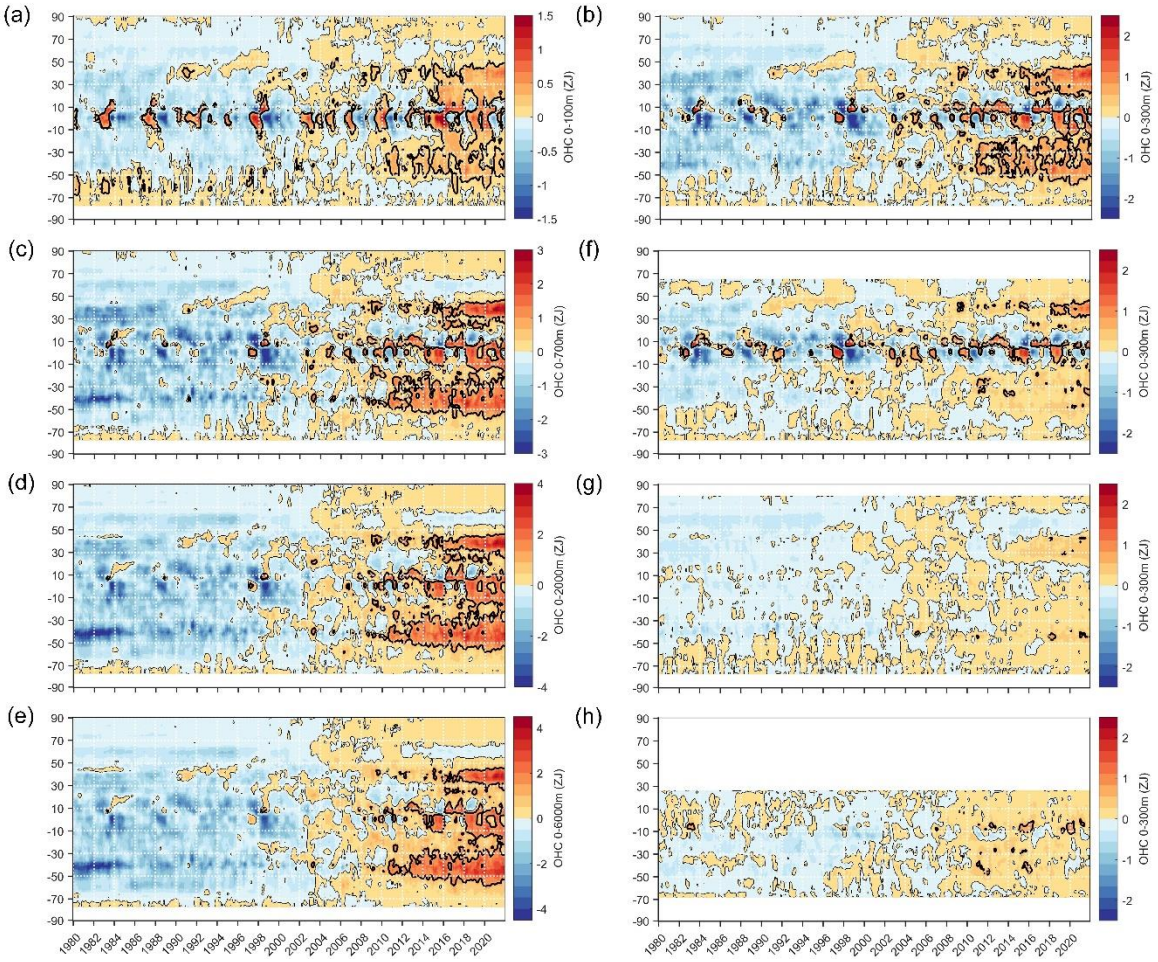

Supplementary Figure 25 Zonal variations of accumulated ocean heat content (OHC) anomalies relative to 2001-2010 at different depths at ocean basins. a-e, global accumulated OHC variations at depths of 0-100m, 0-300m, 0-700m, 0-2000m, and 0-6000m, respectively. **f-h**, accumulated OHC variations at 0-300m for Pacific, Atlantic, and Indian Oceans. The thick black lines highlight the significant increase of OHC, with increased magnitudes of > 0.2 ZJ at 0-100m, > 0.5 ZJ at 0-300m, > 0.7 ZJ at 0-700m, >1.0 ZJ at 0-2000m, and > 1.3 ZJ at 0-6000m, respectively.

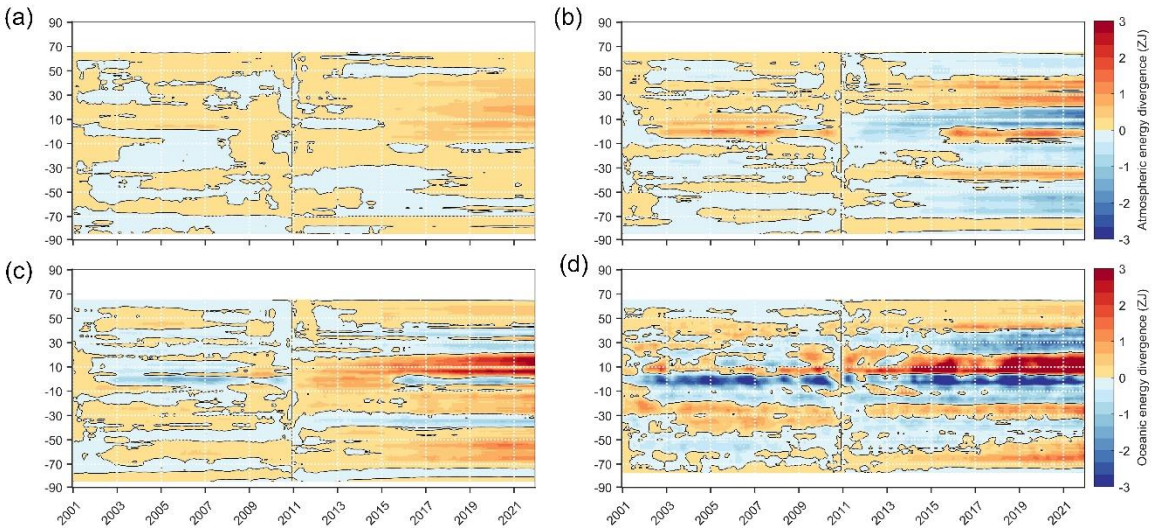

Supplementary Figure 26. Zonal variations of accumulated energy fluxes relative to the base period of 2001-2010 from the TOA to surface at Pacific Ocean. a, TOA net radiative energy flux down. **b,** vertically integrated atmospheric energy flux divergence (TEDIV). **c,** inferred zonal mean net surface energy flux. **d,** vertically integrated time integrated ocean heat divergence (OEDIV). The black line is the zero contour.

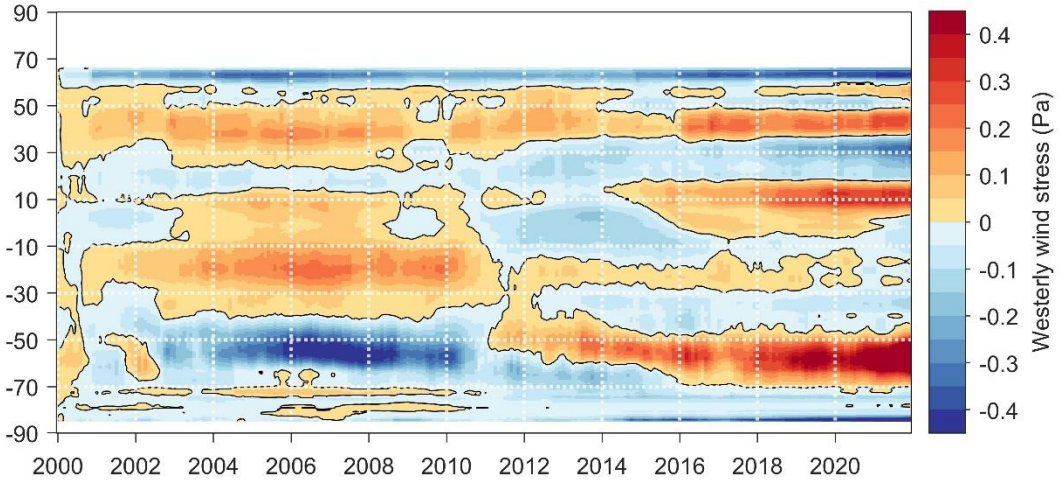

Supplementary Figure 27. Zonal variations of accumulated ocean surface westerly wind stress to a base period of 2001-2010 at the Pacific Ocean. Anomalous zonal mean eastward (westward) wind stress indicates southward (northward) Ekman transports in the Northern Hemisphere but northward (southward) Ekman transports in the Southern Hemisphere.

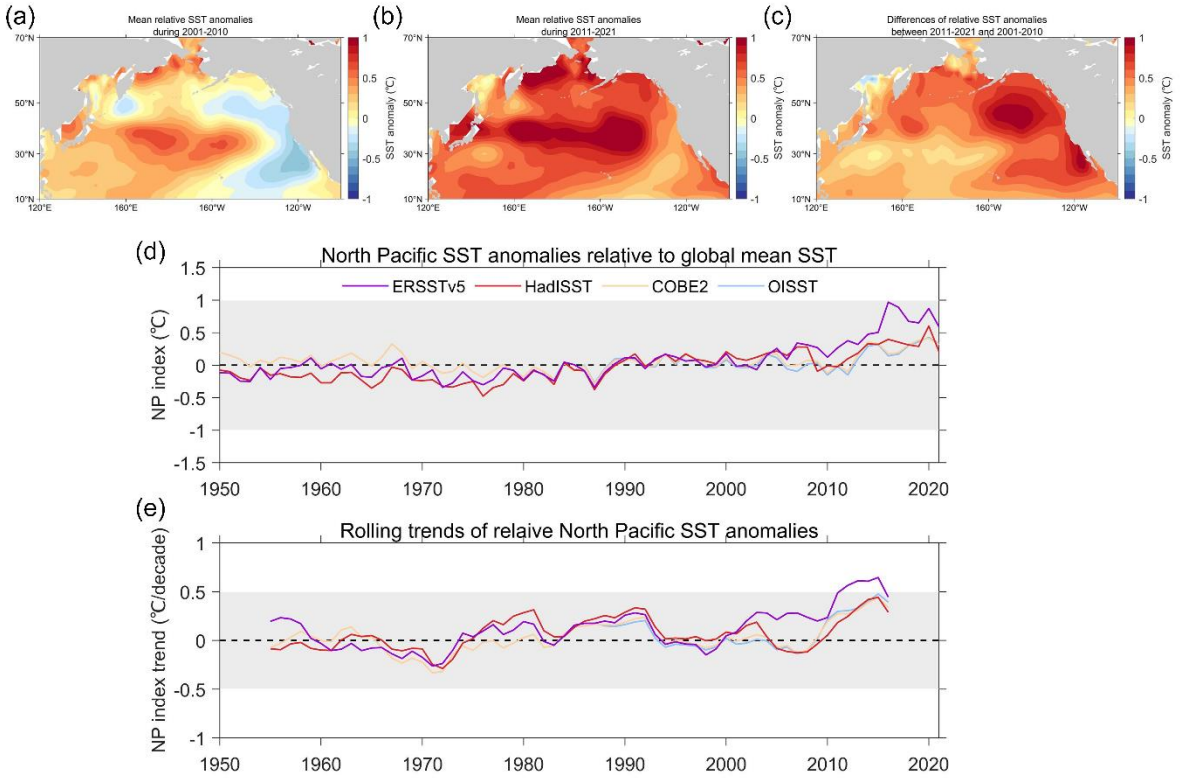

Supplementary Figure 28. Observed North Pacific (NP) warming after 2010. a-b, spatial distribution of the annual mean relative (referenced to the global mean SST) SST anomalies during 2001-2010 and 2011-2021, respectively. **c,** the difference between (b) and (a). **d,** time series of annual mean relative North Pacific (NP) SST index during 1950-2021 from ERSSTv5, HadISST, COBE2, and OISST products. The NP index is defined as the regional mean relative SST anomaly averaged over the NP ocean relative to the global mean SST. **e,** time series of rolling 10-year trends of the annual mean NP index during 1950-2021 in ERSSTv5, HadISST, COBE2, and OISST. The climatology is calculated over the period of 1980-2000.

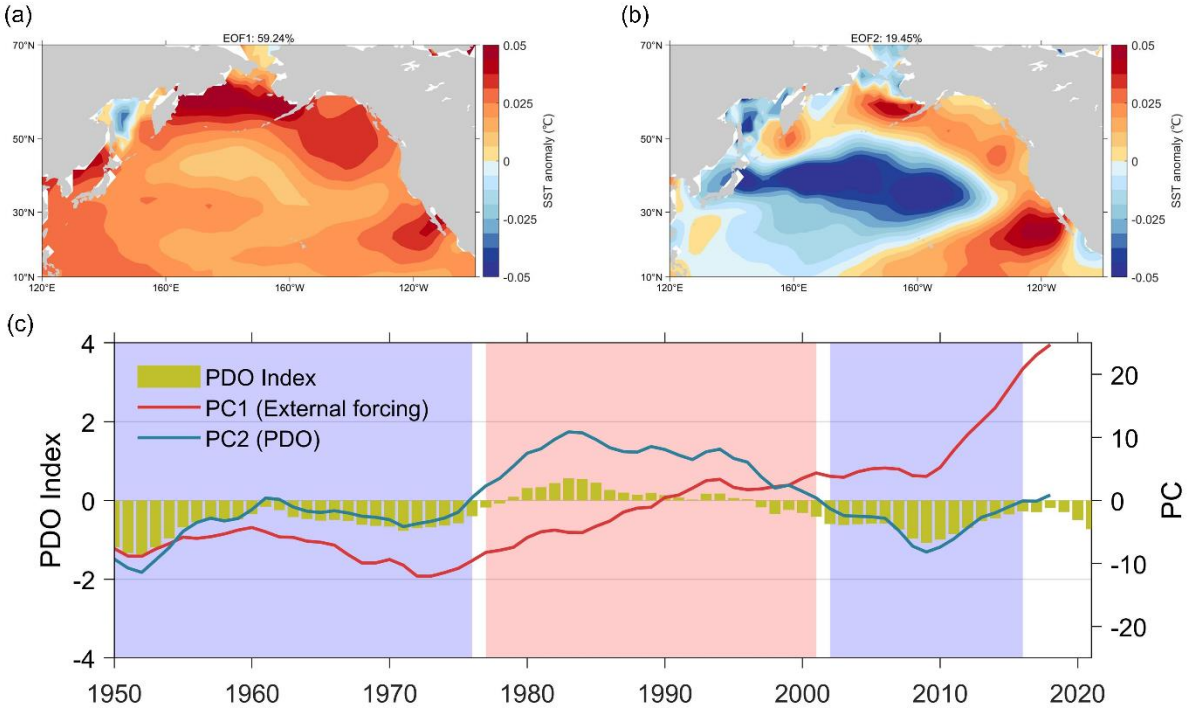

Supplementary Figure 29. Empirical orthogonal function (EOF) decomposition of the North Pacific SST change. a, the first EOF1 of low-pass filtered annual mean SST anomaly during 1950 to 2021. **b,** the second EOF2 of low-pass filtered annual mean SST anomaly during 1950-2021. **c,** the time series of the first two principal components (PCs) of the EOF decomposition during 1950-2021 and the low-pass filtered Pacific Decadal Oscillation (PDO) index. The explained variances of the first two PCs are reported on the top of the (a-b) panels. The sign of PDO warm and cold phases are shaded in red and bule in panel (c). The climatology is constructed over the period of 1980-2000. ERSSTv5 SST is used to perform EOF analysis.

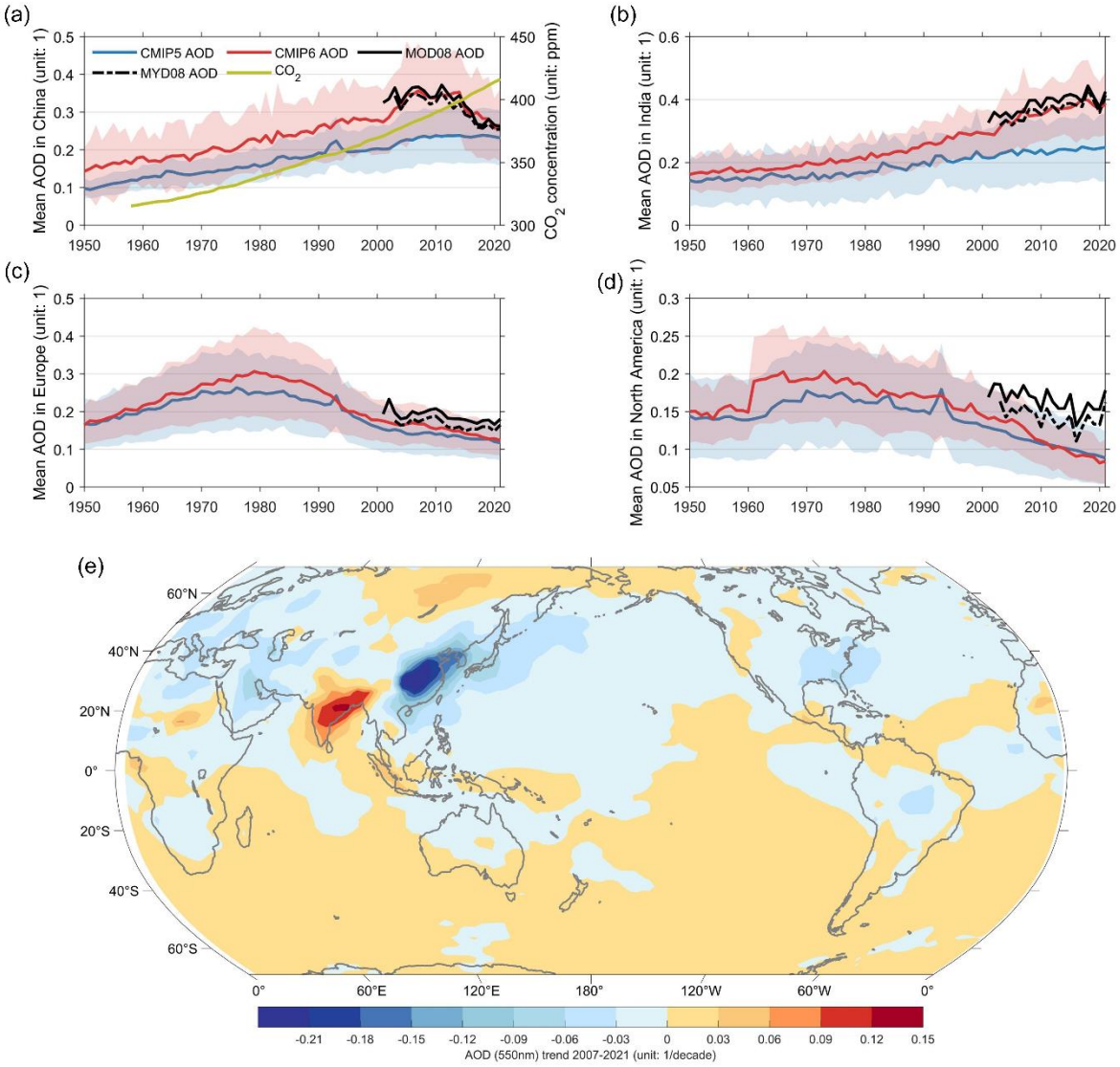

Supplementary Figure 30. Observed and simulated changes in aerosol emissions. a, annual mean 550 nm AOD change in the MODIS observations (black), the CMIP6 all-forcing simulations extend using simulations under the SSP2-4.5 scenario (red), and the CMIP5 all-forcing simulations extended using simulations under the RCP5.4 scenario (blue) during the 1950-2021 in the East China. Solid lines are the multi-model ensemble means and shadings represent the intermodal spreads with one standard deviation. The green line represents the observed CO_2 concentration. **b-d,** same as **a** but in the India, Europe, and North America, respectively. **e,** spatial distribution of trend in annual mean MODIS 550 nm AOD during 2007-2021.

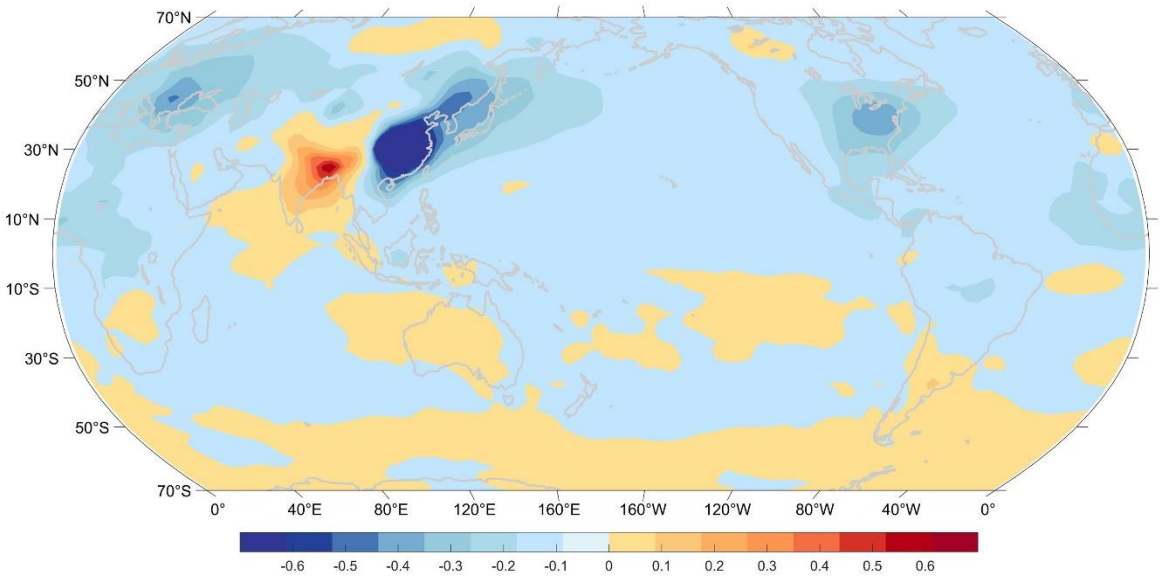

Supplementary Figure 31. Regressions of 550 nm AOD onto the relative NP SST anomalies in CMIP6 aerosol-forcing simulations. The linear regressions are performed during the 1950-2020 period. The climatology is constructed over the period of 1950-2000.

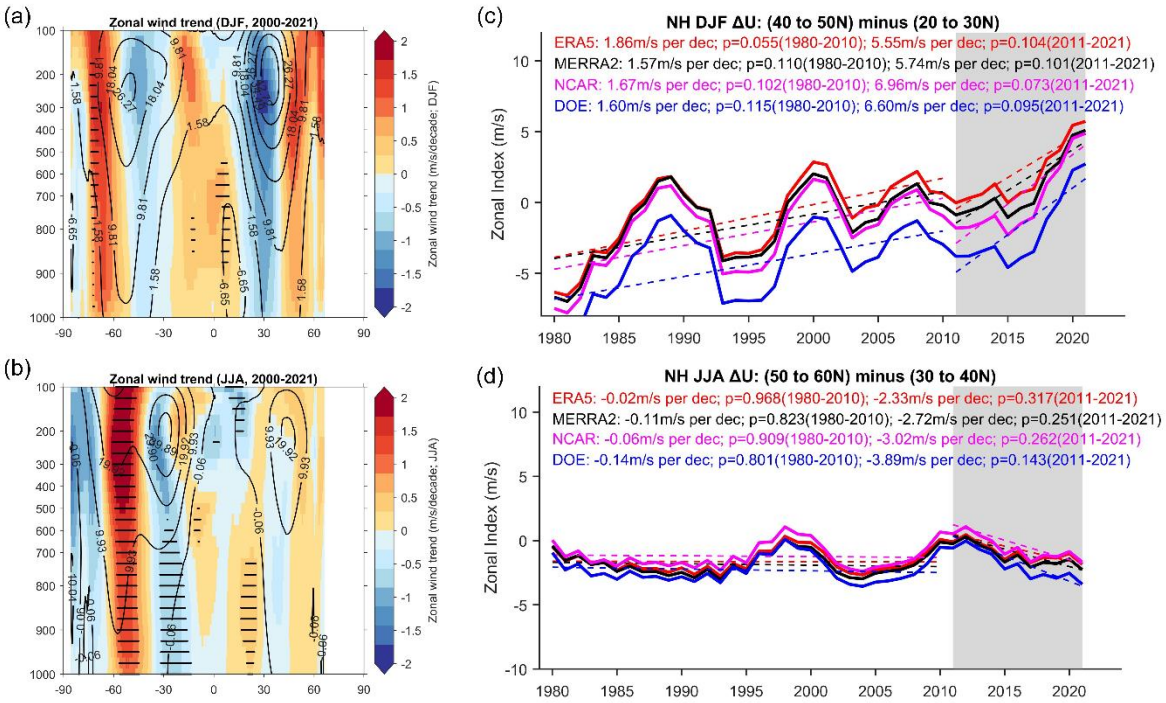

Supplementary Figure 32. Enhanced poleward shifting atmospheric jet streams over the North Pacific. a, linear trends in winter (December-January-February; DJF) zonal mean winds from ERA5 during 2000-2021. **b**, same as **a** but for summer (Jun-July-August; JJA). **c, d** winter and summer zonal indices of characterizing the zonal wind trends at 500 hPa from four reanalyses in the North Pacific. Trends are calculated using the linear least squares regression. Black dots indicate significance at the 5% level using a T-test. Solid lines mark the climatology of zonal winds and temperatures. Shaded area indicates the period of 2011-2021. The four reanalyses data include ERA5, MERRA2, NCEP-NCAR, and NCEP-DOE. An obvious trend in the poleward atmospheric jet was observed in the NP winter zonal wind after 2010.

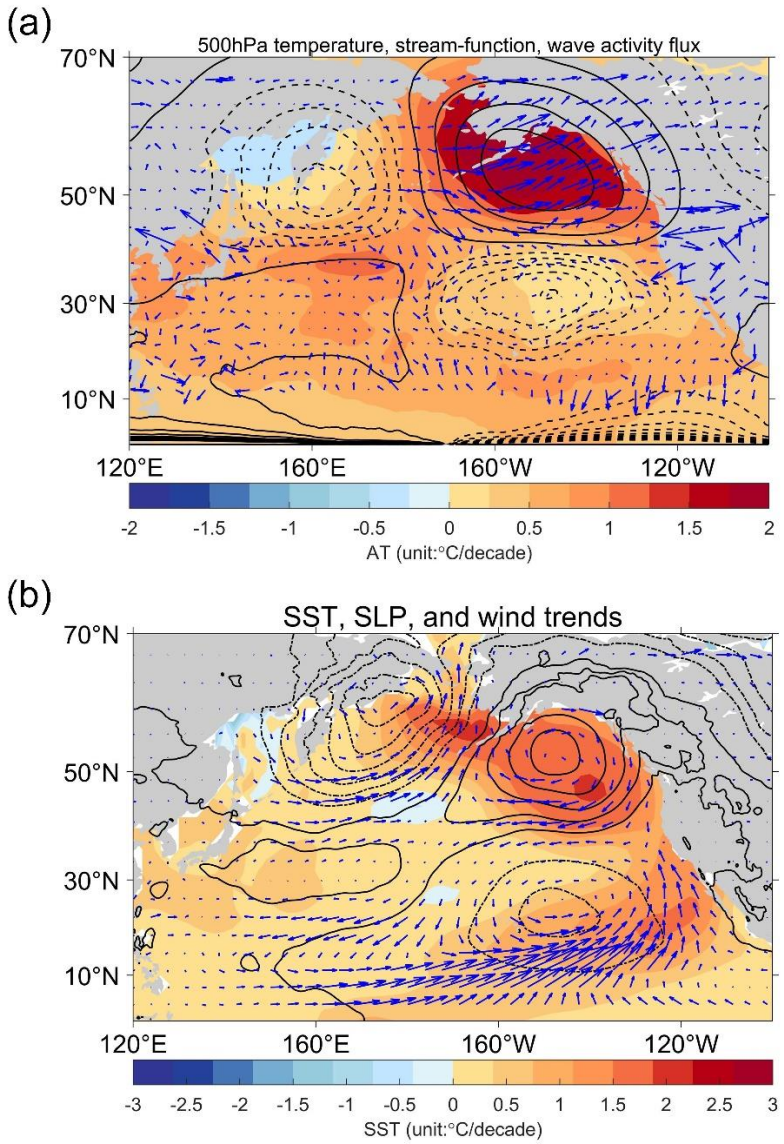

Supplementary Figure 33. Atmosphere teleconnections from reduced aerosol emissions in China induces anomalous eastern North Pacific warming. a, trends of annual mean 500 hPa atmospheric temperature (shading, warm colors indicate an increasing trend, while cool colors indicate a decreasing trend), stream-function (contours, solid contours represent clockwise circulation anomalies and dashed contours represent anticlockwise circulation anomalies), and wave-activity fluxes (vectors, the length of the vector indicates the magnitude of the flux, and the direction of the vector indicates the direction of flux flow) during 2007-2021. **b,** trends of annual mean sea surface temperature (shading, warm colors indicate an increasing trend, while cool colors indicate a decreasing trend), sea level pressure (contours, solid contours denote high-pressure anomalies and dashed contours denote low-pressure anomalies), and surface wind stress (vectors, the length of the vector indicates the magnitude of wind speed, and the direction of the vector indicates the direction of wind speed) during 2007-2021. The climatology is constructed during the period of 2001-2010.

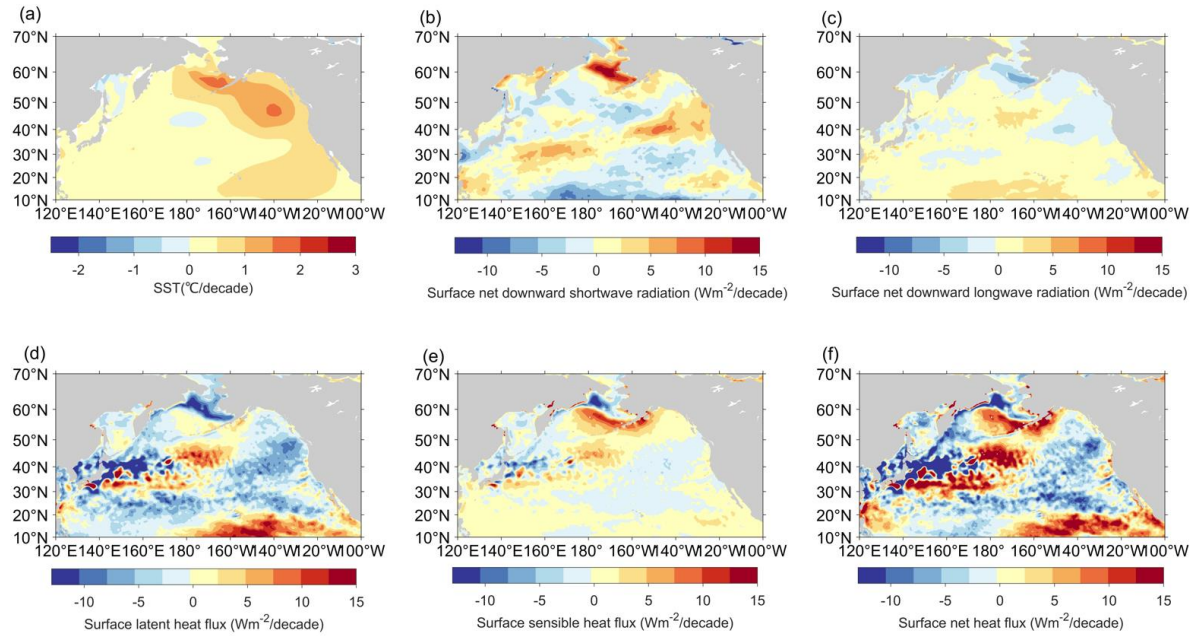

Supplementary Figure 34. Observed North Pacific SST warming and the corresponding heat flux trends during 2007-2021. a, annual mean sea surface temperature trends. **b,** annual mean surface net shortwave radiation trends. **c,** annual mean surface net longwave radiation trends. **d,** annual mean surface latent heat flux trends. **e,** annual mean surface sensible heat flux trends. **f,** annual mean surface net heat flux trends. The SST trends are calculated from ERSSTv5 and radiation and heat fluxes trends are derived from ERA5. The radiation and heat fluxes are positive downward.

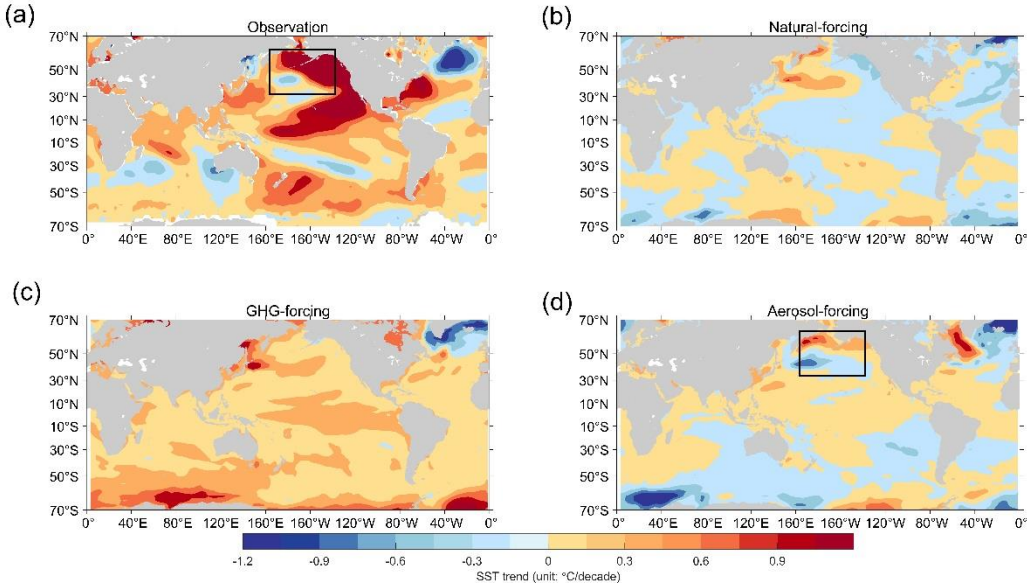

Supplementary Figure 35. Sea surface temperature trends for the 15-year period 2007 to 2021. a-d, observations (ERSSTv5) are compared with CMIP6 model simulations of the effects of natural factors (volcanoes and solar variations) (**b**), GHGs (**c**), and anthropogenic aerosols (**d**). Units are °C per decade. The boxes in **a, d** show the Aleutian Low region (160°–220°E, 30°–65°N).

Supplementary Table 1. List of the 23 CMIP6 ensemble models used in this study.

CMIP6 models	Institute/Country	Horizontal resolution (lat. × lon.)	Variant label
ACCESS-CM2	CSIRO/Australian	1.25° × 1.875°	r1i1p1f1
ACCESS-ESM1-5	CSIRO/Australian	1.25° × 1.875°	r1i1p1f1
AWI-CM-1-1-MR	AWI/Germany	0.94° × 0.94°	r1i1p1f1
CAMS-CSM1-0	CAMS/China	1.125° × 1.125°	r1i1p1f1
CAS-ESM2-0	CAS/China	1.41° × 1.41°	r1i1p1f1
CMCC-CM2-SR5	CMCC/Italy	0.94° × 1.25°	r1i1p1f1
CMCC-ESM2	CMCC/Italy	0.94° × 1.25°	r1i1p1f1
CanESM5-1	CCCma/Canada	2.81° × 2.81°	r1i1p1f1
E3SM-1-1	E3SM-Project/USA	1.0° × 1.0°	r1i1p1f1
EC-Earth3-Veg	EC-Earth-Consortium/ Sweden	0.70° × 0.70°	r1i1p1f1
EC-Earth3-Veg-LR	EC-Earth-Consortium/ Sweden	0.06° × 1.125°	r1i1p1f1
FGOALS-g3	CAS/China	2.25° × 2.0°	r1i1p1f1
FIO-ESM-2-0	FIO-QLNM/China	0.94° × 1.25°	r1i1p1f1
IITM-ESM	CCCR-IITM/India	1.91° × 1.875°	r1i1p1f1
INM-CM4-8	INM/Russia	1.50° × 2.0°	r1i1p1f1
INM-CM5-0	INM/Russia	1.50° × 2.0°	r1i1p1f1
IPSL-CM6A-LR	IPSL/France	1.26° × 2.5°	r1i1p1f1
MIROC6	MIROC/Japan	1.41° × 1.41°	r1i1p1f1
MPI-ESM1-2-HR	DKRZ/Germany	0.94° × 0.94°	r1i1p1f1
MPI-ESM1-2-LR	DKRZ/Germany	1.875° × 1.875°	r1i1p1f1
MRI-ESM2-0	MRI/Japan	1.125° × 1.125°	r1i1p1f1
NorESM2-LM	NCC/Norway	1.875° × 2.5°	r1i1p1f1
NorESM2-MM	NCC/Norway	0.94° × 1.25°	r1i1p1f1

Note that most of the models have irregular grids and the resolution quoted in the table are approximate.

Supplementary Table 2. The CMIP6 and CMIP5 models used in attribution of the North Pacific anomalous warming

CMIP6	CMIP5	Institution
ACCESS-CM2	ACCESS1-0	Commonwealth Scientific and Industrial Research Organisation, Australia,
ACCESS-ESM1-5	ACCESS1-3	Australian Research Council Centre of Excellence for Climate System Science
CanESM5	CanESM2	Canadian Centre for Climate Modelling and Analysis, Environment and Climate Change Canada, Canada
CNRM-CM6-1	CNRM-CM5	Centre National de Recherches Meteorologiques, France
FGOALS-g3	FGOALS-s2	Chinese Academy of Sciences, China
GFDL-ESM4	GFDL-CM3	National Oceanic and Atmospheric Administration, Geophysical Fluid Dynamics Laboratory, USA
HadGEM3-GC31-LL	HadGEM2-CC	Met Office Hadley Centre, UK
IPSL-CM6A-LR	IPSL-CM5A-LR	Institut Pierre Simon Laplace, France
MIROC6	MIROC5	Japan Agency for Marine-Earth Science and Technology, Japan
MRI-ESM2-0	MRI-CGCM3	Meteorological Research Institute, Japan
NorESM2-LM	NorESM1-M	NorESM Climate modeling Consortium consisting of Center for International Climate and Environmental Research

Supplementary Table 3. Climate models used in the calculation of sea surface temperature pattern effect from AMIP-series experiments.

Model	Institute/Country (region)	Variant label
BCC-CSM2-MR	Beijing Climate Center, China	r1i1p1f1
CESM2	National Center for Atmospheric Research, United States	r1i1p1f1
IPSL-CM6A-LR	Institut Pierre-Simon Laplace, France	r1i1p1f1
MIROC6	Japan Agency for Marine-Earth Science and Technology, Japan	r1i1p1f1
MRI-ESM2-0	Japan Meteorological Agency, Japan	r1i1p1f1
TaiESM1	Research Center for Environmental Changes, Taiwan	r1i1p1f1

Supplementary Text 1: Bayesian model averaging

An important strategy in this study is the differentiation of CMIP6 ensemble models. To obtain an accurate 40-year EEB record, it is necessary to reduce the impact of poorly predicting ESMs simulations on the integrated results through the CERES-EBAF observation constraints, while giving larger weights to climate models with superior simulations. Regarding the task, the Bayesian Model Averaging (BMA) is a highly effective method based on the Bayesian statistics. Unlike traditional model selection (e.g., choosing a single best model or simple averaging of multiple ESMs), the BMA balances and integrates predictions from multiple models or hypotheses while retaining the uncertainty inherent in the multi-model approach[2]. Therefore, the BMA method is utilized to merge the EEB simulated data from 23 CMIP6 climate models with CERES-EBAF observation constraints to generate accurate EEB records in the last four decades.

The fundamental concept of the BMA is to consider all possible models and assign each a weight proportional to how well the model matches the reference data (CERES observations). The weight is the model's posterior probability, which combines its prior probability with its likelihood given the data[3, 4]. The BMA method improves the accuracy of EEB simulations by modifying the predictive probability density function (PDF) to achieve a good fit to the observational CERES-EBAF EEB data.

Specifically, the BMA method considers a predictive variable *y*, the corresponding CERES data at a given time $t(y_t)$, and an ensemble ESMs $F\{M_1, M_2, \dots, M_f\}$ for variable *y*. In this study, *y* refers to predicted EEB component and *f* equals to 23. The law of total probability tells us that the predictive *PDF*, *p(y)*, can be expressed as

$$p(y|M_1, M_2, \dots, M_f) = \sum_{i=1}^{f} p(y|M_i) \times p(M_i|y_t) \quad (1)$$

where $p(y|M_i)$ is the predictive PDF using model M_i alone and $p(M_i|y_t)$ denotes the posterior probability that ESM (M_i) is correct given the corresponding CERES-EBAF data. Generally, $p(M_i|y_t)$ can be considered as a statistical weight u_i, reflecting how well M_i matches the CERES-EBAF data, and $\sum_{i=1}^{f} u_i = 1$. Thus, equation (1) can be alternatively expressed as

$$p(y|M_1, M_2, \dots, M_f) = \sum_{i=1}^{f} u_i \times p(y|M_i) \quad (2).$$

$p(y|M_i)$ is assumed to meet a normal distribution[5, 6] defined by a mean $\widetilde{M}_i$ and a variance ω_i^2. Assuming the parameter vector $\theta_i = \{\widetilde{M}_i, \omega_i^2\}$ and a conditional density function $h(\cdot)$ as the *PDF* associated with the normal distribution, this can be written as

$$p(y|M_i) = h(y|\theta_i) \tag{3}$$

We combine equations (2) and (3) and obtain

$$p(y|M_1, M_2, \dots, M_f) = \sum_{i=1}^{f} u_i \times h(y|\theta_i) \tag{4}$$

The conditional expectation (*E*) of *y* is the ultimate BMA predictive EEB for merging 23 ESM simulations and can be expressed as

$$E(y|M_1, M_2, \dots, M_f) = \sum_{i=1}^{f} u_i \times \widetilde{M}_i \tag{5}$$

where $\widetilde{M}_i$ is the simulated EEB from individual models. To obtain both u_i and θ_i, a log likelihood function (*I*) from the Gaussian function *h* on the basis of training CERES-EBAF data can be used. The log likelihood function is summed over all spatial points (s) and time points (t) as follows

$$I(\theta_1, \theta_2, \dots, \theta_f) = \sum_{(s,t)} log\left[\sum_{i=1}^{f} u_i \times h(y_{s,t}|\theta_i)\right] \tag{6}$$

where $\sum_{(s,t)}$ refers to the summation of CERES-EBAF EEB values; $y_{s,t}$ is a CERES-EBAF EEB value at location *s* and time *t*. The BMA method estimates the Bayesian weights u_i and parameter vector θ_i when the log likelihood function *I* is maximized. We maximize the log likelihood function *I* using the expectation-maximization (EM) algorithm[6].

Practically, the bilinear interpolation method is first used to resample the EEB simulations from 23 ESMs into 1°×1° horizontal resolution, consistent with the spatial resolution of the CERES-EBAF product. The integration process is then conducted pixel by pixel on a monthly basis to ensure the quality of the CERES-ESM EEB dataset,

$$\text{CERES} - \text{ESM}_{i,j,m}^{integ} = BMA\left(EEB_{i,j,m}^{ESM1}, EEB_{i,j,m}^{ESM2}, \dots\dots, EEB_{i,j,m}^{ESM23}\right) \tag{7}$$

where $\text{CERES} - \text{ESM}_{i,j,m}^{integ}$ is the integrated EEB values; $EEB_{i,j,m}^{ESM1}$ is the ESM-simulated EEB; *i*, *j*, and *m* represent the latitude, longitude, and month of the ESM cell, respectively. The cross-validation scheme was applied to obtain robust weights and then a 23 ESMs-merged EEB record was produced using the pre-determined weights. Compared with independent EEB data

from other satellite and reanalysis sources (e.g., CLARA-A3, ERA5, and DEEP-C), the comparison results show that the integrated CERES-ESM EEB dataset has a better agreement with the CERES-EBAF product. More detailed evaluations on the CERES-ESM dataset are provided in the Supplementary Text 2.

Supplementary Text 2: Evaluation of the CERES-ESM Earth energy budget in accuracy validations, temporal variabilities, and trend comparisons.

The BMA method was applied to generate the 40-yr CERES-ESM EEB dataset. To illustrate the advantages of the CERES-ESM dataset in terms of data accuracy, spatiotemporal distributions, and trends, four datasets, including CMIP6, CLARA-A3, ERA5, and DEEP-C, are used for inter-comparisons against the CERES-EBAF baseline. Multiple evaluation indicators were selected to comprehensively evaluate the quality of the CERES-ESM dataset, including bias, relative bias, root mean square error (RMSE), relative RMSE, coefficient of determination (R^2):

$$BIAS = \frac{1}{N}\sum_{i=1}^{N}(x_i - x_i') \quad (8)$$

$$RMSE = \sqrt{\frac{1}{N}\sum_{i=1}^{N}(x_i - x_i')^2} \quad (9)$$

$$R^2 = \frac{\sum_{i=1}^{N}(x_i' - \bar{x})^2}{\sum_{i=1}^{N}(x_i - \bar{x})^2} \quad (10)$$

where x_i, x_i', and $\bar{x}$ are observed, predicted, and mean values of the targeted parameter, respectively; N is the number of samples.

Regarding absorbed solar radiation (ASR), CERES-ESM exhibits lower uncertainty and smaller bias than DEEP-C, ERA5, and CMIP6 ensemble multi-model mean, with a bias of 0.20 Wm^{-2} and an RMSE of 4.70 Wm^{-2} (Supplementary Figure 2). CERES-ESM outgoing longwave radiation (OLR) also shows an accuracy advantage, with a bias of 0.01 Wm^{-2} and an RMSE of 0.95 Wm^{-2}. These values for the remaining four datasets exceed 0.4 Wm^{-2} for bias and 2.5 Wm^{-2} for RMSE, respectively (Supplementary Figure 3). Therefore, CERES-ESM EEI has the highest accuracy, characterizing a bias of 0.19 Wm^{-2}, an RMSE of 4.59 Wm^{-2}, and an R^2 of 1.00 (Supplementary Figure 4). Therefore, the CERES-ESM has better accuracy than several mainstream EEB products based on the global validation results.

The trends in EEB fluxes at the pixel level are inter-comparisons to assess how well the CERES-ESM datasets capture the temporal variabilities of the local EEB fluxes. The CERES-ESM and DEEP-C ASR show comparable performances in characterizing the temporal variabilities of EEB fluxes at the pixel level, outperforming the ERA5 and CMIP6 ensemble multi-model mean, with RMSEs of 0.59 and 0.56 $Wm^{-2}decadel^{-1}$ and biases of -0.14 and -0.07 $Wm^{-2}decadel^{-1}$ (Supplementary Figure 5). Regarding the OLR, CERES-ESM performs best in

capturing the long-term trend of local OLR flux, with an RMSE of 0.18 $Wm^{-2}decadel^{-1}$ and a bias of 0.00 $Wm^{-2}decadel^{-1}$ (Supplementary Figure 6). Second place goes to the DEEP-C product (bias = 0.02 $Wm^{-2}decadel^{-1}$, RMSE = 0.27 $Wm^{-2}decadel^{-1}$). Similar to ASR, CERES-ESM has a comparable performance with the DEEP-C product in capturing the temporal variability of EEI at the pixel level, with an RMSE of 0.58 $Wm^{-2}decadel^{-1}$ and a bias of -0.14 $Wm^{-2}decadel^{-1}$ (Supplementary Figure 7). CERES-ESM and DEEP-C data are generally better able to depict the long-term trend of EEB at the local scale than the other three datasets.

The time series of EEB anomalies from the five datasets at both regional and global scales are further inter-compared to fully examine whether the CERES-ESM is suitable for analyzing the long-term variabilities of EEB at a large spatial scale. The globe is divided into 13 land and ocean basin regions by referencing the climatology of NASA Energy and Water cycle Study (NEWS)[7] to comprehensively investigate the quality of the CERES-ESM dataset. Regarding ASR, there exists a great temporal consistency between the five datasets at both global and regional scales before ~2012, but ERA5 ASR is smaller than the other four datasets by ~0.7 Wm^{-2} after 2012 at the global scale. Regionally, the noticeable underestimation of ERA5 ASR is found over the Eastern Pacific Ocean off North America (Supplementary Figure 8). CERES observes large positive ASR trends over this region, which is associated with a reduction of low-cloud cover; however, ERA5 shows negative ASR trends throughout most of the Eastern Pacific Ocean off North America[8]. The discrepancy implies that the low-cloud response to SST increase is insensitive in the ERA5 numerical weather prediction (NWP) model. In addition, the time series of OLR anomalies from the five datasets have great agreements at both regional and global scales (Supplementary Figure 9). However, ERA5 OLR differs greatly from the CERES-ESM and DEEP-C in the years 1992 and 1998 with a strong volcanic eruption and an extreme ENSO event. This also implies that the ERA5 NWP model for calculating EEB cannot respond to these natural forcing agents well in the assimilation process. Accordingly, the EEI records from CERES-EBAF, CERES-ESM, and DEEP-C have better temporal consistency than those from ERA5. The CERES-ESM EEB datasets overall have reasonable temporal variabilities at both regional and global scales by comparing with the other five EEB products.

Based on the above evaluations (accuracy, local trends, and long-term variabilities at both regional and global scales), the CERES-ESM EEB dataset has presented a great potential for

examining the spatiotemporal variabilities of the EEB fluxes across different spatial and temporal scales. Therefore, the CERES-ESM EEB is used as the data basis in the following analysis to examine the spatiotemporal variabilities of the Earth's energy budget.

Supplementary Text 3: Radiative forcings and climatical responses over different periods

Following the shifts in the trends of EEB fluxes, the 40-year EEB records are split into segments to better understand the underlying forcings and responses of the TEEI at different periods (Supplementary Figure 15). The rapid adjustments (ΔA_x) and radiative responses ($\lambda \Delta T_s$) from temperature (T), water vapor (q), surface albedo (α), and cloud (C) changes are separated from the total radiative change (ΔR_x). The radiative response ($\lambda \Delta T_s$) is also decomposed into different surface and atmospheric processes. The ASR trend in radiative response (0.38 ± 0.03 $Wm^{-2}decade^{-1}$) contributes mostly to the total increasing TEEI (0.33 ± 0.05 $Wm^{-2}decade^{-1}$) for the 1980–2021 period, partly neutralized by the ASR trend in ERF and the OLR trend in $\lambda \Delta T_s$. The cloud shortwave feedback is the most significant process (0.23 ± 0.02 $Wm^{-2}decade^{-1}$) for explaining the positive ASR trend. The negative trends in the ASR *ERF* and OLR $\lambda \Delta T_s$ are mainly attributed to cloud rapid adjustment and the Earth's Planck response due to the increased GMST.

During the 1980–2000 period, the positive TEEI (0.51 ± 0.16 $Wm^{-2}decade^{-1}$) is mostly attributed to the lesser OLR (0.43 ± 0.13 $Wm^{-2}decade^{-1}$), due to the positive ERF (0.53 ± 0.12 $Wm^{-2}decade^{-1}$). The first two decades were split into 1984–1990 and 1994–2000 to exclude years with the effect of strong volcanic eruptions. The ASR trend in $\lambda \Delta T_s$ (0.73 ± 0.41 $Wm^{-2}decade^{-1}$) mostly contributes to the positive TEEI (0.67 ± 0.70 $Wm^{-2}decade^{-1}$) at the 1984–1990 period. The feedbacks of surface albedo (0.24 ± 0.15 $Wm^{-2}decade^{-1}$) and cloud cover (0.30 ± 0.37 $Wm^{-2}decade^{-1}$) contribute largely to the total ASR $\lambda \Delta T_s$ during this period. The two processes correspond to the reduced snow/ice cover, a recovery from the 1982 El Chichón volcanic aerosol, and declining aerosol–cloud interactions in Europe[9].

For the period of 1994–2000, the positive TEEI (1.18 ± 0.62 $Wm^{-2}decade^{-1}$) is largely attributed to the OLR ERF (1.69 ± 0.51 $Wm^{-2}decade^{-1}$). The ΔA_C for the external IRF (1.27 ± 0.42 $Wm^{-2}decade^{-1}$) largely contributes to the large positive OLR trend in total ERF. The powerful 1997–2000 ENSO is the strongest perturbation accounting for the external IRF. Most of the positive trends of ΔA_C in OLR are found at the western Pacific warm pool due to an increase of high-level clouds (Supplementary Fig. 16c). This process responds to the increased SST at the western warm pool due to the 1998–2000 La Niña event. A high consistency of temporal variations between rapid cloud adjustment and high-level cloud cover (r = 0.88)

illustrates the significant perturbation of La Niña on the TEEI at this period. The intensity of the 1991 Pinatubo volcanic eruption is larger than that of 1982 El Chichón, causing a larger radiative response of cloud in ASR (0.60 ± 0.28 $Wm^{-2}decade^{-1}$). However, this radiative heating effect is counterbalanced by the shortwave cooling effect of cloud (-1.24 ± 0.52 $Wm^{-2}decade^{-1}$) in rapid adjustment for this perturbation; the 1997–2000 ENSO becomes the most significant forcing to affect the TEEI during the 1994–2000 period.

TEEI from 2001 to 2021 (0.40 ± 0.14 $Wm^{-2}decade^{-1}$) is mostly determined by the positive trend of ASR (0.64 ± 0.11 $Wm^{-2}decade^{-1}$), which is different from the 1980–2000 period. Specifically, the TEEI from 2011–2016 contributes most to the TEEI in the recent two decades. During the 2011–2016 period, the ASR trend in radiative response (1.12 ± 0.43 $Wm^{-2}decade^{-1}$) is the most significant process shaping the positive TEEI. The contributions from surface albedo (0.34 ± 0.22 $Wm^{-2}decade^{-1}$, 30%) and cloud cover (0.61 ± 0.28 $Wm^{-2}decade^{-1}$, 54%) contribute most of the ASR change in total shortwave radiative response. The warming effect in surface albedo radiative response is due to the significant reduction of snow/ice cover in 2015 when there is a strong El Niño event (Supplementary Figure 17).

The reduced low-level cloud cover, on the other hand, is the main cause for the increase of cloud shortwave radiative response during 2011–2016 (Supplementary Figure 18). The strong 2015/16 El Niño led to a significant increase of SST in the eastern Pacific oceans, enhancing the air-sea interaction and reducing lower tropospheric stability (decreased estimated inversion strength). In the central and eastern Pacific oceans, high-level cloud increases and low-level cloud decreases as a result of strong deep convection. Change in low cloud-mediated radiative response is essentially attributed to the El Niño-induced SST increase ($r = 0.96$). Natural forcing generally appears to be the main perturbation to the variations of EEB at short-term periods, in contrast to long-term global warming, most of which is of anthropogenic origin.

There is a discernible difference between 1994–2000 and 2011–2016 in the response of cloud cover to the ENSO forcing, although the two El Niño events (1997–1998 and 2015–2016) have similar intensities (Nino3.4 > 2 K, Supplementary Fig. 1b). Because of the change in middle- and high-level clouds during 1994–2000 (rapid adjustment), total cloud cover decreased in the central Pacific Ocean and increased in the western warm pool (Supplementary

Figure 16f). In contrast, the change in low-level clouds during the 2011–2016 period (radiative response), on the other hand, caused total cloud cover to increase in the central Pacific oceans and decrease in the western warm pool (Supplementary Figure 18d). Instead of being a forcing agent, the variation in cloud cover is feedback on the increased GMST during 2011–2016. Anomalous ocean warming may play an important role in recent accelerated global warming rate.

Supplementary References

1. Smith C, Hall B, Dentener F, Ahn J, Collins W, Jones C*, et al.* IPCC Working Group 1 (WG1) Sixth Assessment Report (AR6) Annex III Ext ended Data. v1.0 ed: Zenodo; 2021.

2. Li X, Li Q, Wild M, Jones P. An intensification of surface Earth's energy imbalance since the late 20th century. *Communications Earth & Environment* 2024, **5**(1)**:** 644.

3. Raftery AE, Madigan D, Hoeting JA. Bayesian model averaging for linear regression models. *Journal of the American Statistical Association* 1997, **92**(437)**:** 179-191.

4. Hoeting JA, Madigan D, Raftery AE, Volinsky CT. Bayesian model averaging: a tutorial (with comments by M. Clyde, David Draper and EI George, and a rejoinder by the authors. *Statistical science* 1999, **14**(4)**:** 382-417.

5. Raftery AE, Gneiting T, Balabdaoui F, Polakowski M. Using Bayesian model averaging to calibrate forecast ensembles. *Monthly weather review* 2005, **133**(5)**:** 1155-1174.

6. Duan Q, Phillips TJ. Bayesian estimation of local signal and noise in multimodel simulations of climate change. *Journal of Geophysical Research: Atmospheres* 2010, **115**(D18).

7. L'Ecuyer TS, Beaudoing H, Rodell M, Olson W, Lin B, Kato S*, et al.* The observed state of the energy budget in the early twenty-first century. *Journal of Climate* 2015, **28**(21)**:** 8319-8346.

8. Loeb NG, Mayer M, Kato S, Fasullo JT, Zuo H, Senan R*, et al.* Evaluating Twenty-Year Trends in Earth's Energy Flows From Observations and Reanalyses. *Journal of Geophysical Research: Atmospheres* 2022, **127**(12)**:** e2022JD036686.

9. Dutton EG, Christy JR. Solar radiative forcing at selected locations and evidence for global lower tropospheric cooling following the eruptions of El Chichón and Pinatubo. *Geophysical research letters* 1992, **19**(23)**:** 2313-2316.